ALDH3A1-mediated detoxification of reactive aldehydes contributes to distinct muscle responses to denervation and Amyotrophic Lateral Sclerosis progression

Ang Li[1*], Li Dong[1], Xuejun Li[1], Jianxun Yi[1], Jianjie Ma[2], Jingsong Zhou[1*]

[1] Department of Kinesiology, College of Nursing and Health Innovation, University of Texas at Arlington, TX, 76019, USA

[2]Department of Surgery, Division of Surgical Sciences, University of Virginia, Charlottesville, VA, 22903, USA

* Corresponding author

Abstract

Different muscles exhibit varied susceptibility to degeneration in Amyotrophic Lateral Sclerosis (ALS), a fatal neuromuscular disorder. Extraocular muscles (EOMs) are particularly resistant to ALS progression and exploring the underlying molecular nature may deliver great therapeutic value. Reactive aldehyde 4-hydroxynonenal (HNE) is implicated in ALS pathogenesis and ALDH3A1 is an inactivation-resistant intracellular detoxifier of 4-HNE protecting eyes against UV-induced oxidative stress. Here we detected prominently higher levels of *ALDH3A1* in mouse EOMs than other muscles under normal physiological conditions. In an ALS mouse model ($hSOD1^{G93A}$) reaching end-stage, *ALDH3A1* expression was sustained at high level in EOMs, whereas substantial upregulation of *ALDH3A1* occurred in soleus and diaphragm. The upregulation was less pronounced in extensor digitorum longus (EDL) muscle, which endured the most severe pathological remodeling as demonstrated by unparalleled upregulation of a denervation marker *ANKRD1* expression. Interestingly, sciatic nerve transection in wildtype mice induced *ALDH3A1* and *ANKRD1* expression in an inverse manner over muscle type and time. Adeno-associated virus enforced overexpression of *ALDH3A1* protected myotubes from 4-HNE-induced DNA fragmentation, plasma membrane leakage and restored MG53-mediated membrane repair. Our data indicate that *ALDH3A1* may contribute to distinct muscle resistance to ALS through detoxifying reactive aldehydes.

Key words: Reactive aldehydes, aldehyde dehydrogenase, amyotrophic lateral sclerosis, extraocular muscle, nuclear translocation, sciatic nerve transection.

Abbreviations: 4-hydroxy-2-nonenal (4-HNE); acetylcholine receptor (AChR); amyotrophic lateral sclerosis (ALS); extensor digitorum longus (EDL); soleus (SOL), diaphragm (DIA), extraocular muscle (EOM); hindlimb (HL); malondialdehyde (MDA), neuromuscular junction (NMJ), satellite cell (SC).

Introduction

Amyotrophic Lateral Sclerosis (ALS) is a devastating neuromuscular disorder characterized with progression motor neuron death and severe skeletal muscle wasting. Remarkably, extraocular muscles (EOMs) controlling eyeball movements exhibit superior preservation of structure, neuromuscular junction (NMJ) integrity and function than many other muscles in ALS patients and rodent models [1-5]. Beside EOMs, animal model studies also show that limb and body muscles respond to ALS progression differently, with fast-twitch muscles generally more susceptible to degeneration than in slow-twitch muscles [6-8]. Factors underlying this phenomenon can be multi-faceted and could hold clues for identifying novel therapeutic targets against muscle degeneration in ALS or other neuromuscular disorders.

Reactive aldehydes resulting from oxidative stress are involved in the pathological process of multiple late-onset neurodegenerative disorders including ALS [9]. One major route for intracellular production of reactive aldehydes is the peroxidation of polyunsaturated fatty acids (PUFA), which are the major component of the cellular membranous structures [10, 11]. Well-known examples include 4-hydroxynonenal (4-HNE), malondialdehyde (MDA) and acrolein [11], which can form adducts with protein through Michael addition or Schiff base formation [12-14]. These adducts contribute to protein crosslinking and aggregation [11], leading to broad pathological consequences including disrupted cell signaling, altered gene expression, inhibited enzyme activity, compromised mitochondrial function and disformed cytoskeleton [15]. Reactive aldehydes can also form adducts with DNA, which can result in inter-strand crosslinks, base substitution, mutation and fragmentation [16-22]. Elevated levels of lipid peroxidation markers, such as 4-HNE adducts, have been detected in cells of central nervous system and body fluids from patients and/or models of amyotrophic lateral sclerosis (ALS), Alzheimer disease (AD), Parkinson disease (PD) and Huntington disease (HD) [9].

To fight against reactive aldehydes, the human body has deployed a series of detoxification enzymes, such as aldehyde dehydrogenase (ALDHs) aimed to oxidize the carbonyl group into corresponding acids, as well as aldo-keto reductase (AKR) aimed to reduce aldehydes into corresponding alcohols [12]. ALDH2, ALDH1A1 and ALDH3A1 are the three most studied ALDHs [23]. ALDH2 is a mitochondrial ALDH abundantly present in liver, brain, heart and muscle [24]. ALDH1A1 and ALDH3A1 are primarily cytosolic and are extremely abundant in mammalian corneal and lens to protect against ultraviolet radiation (UVR) induced generation of reactive aldehydes and their pathological consequences [20, 25, 26]. ALDH3A1 knockout mice and ALDH1A1/ALDH3A1 double knockout mice develop cataracts by 1 month of age [26]. It is also worth noticing that a kinetics study of these three ALDHs reported that ALDH2 was irreversibly inactivated by 4-HNE and acrolein at slightly above 10 μM. ALDH1A1 was inactivated by acrolein at concentrations higher than 1 mM, while no inactivation of ALDH3A1 was observed by either 4-HNE, acrolein or MDA even at 20 mM [23]. Thus, ALDH3A1 is the most inactivation-resistant isoform of the three and the focus of the current study.

It is unknown whether aldehyde dehydrogenases are involved in varied susceptibility of different muscles to degeneration under ALS. Here we examined the expression of *ALDH1A1* and *ALDH3A1* in EDL, soleus, diaphragm and EOMs of hSOD1^{G93A} (G93A) mice, a well-established ALS rodent model [27]. There were little differences in *ALDH1A1* expression between different muscles and disease state. In contrast, *ALDH3A1* expression was dramatically higher in EOMs compared to other muscles in WT mice. Meanwhile it was prominently induced in soleus and diaphragm in G93A mice. The induction was much less pronounced in EDL muscle, which suffers the most severe NMJ degeneration in these four muscle types in G93A mice [5]. Indeed, the commonly used denervation

marker *ANKRD1* [28, 29] was induced most in G93A EDL muscle, suggesting that the expression level of *ALDH3A1* is inversely linked to the severity of muscle pathological remodeling. The distinct expression pattern of *ALDH3A1* gene was also confirmed at the protein level and the pathologically elevated ALDH3A1 protein exhibit enrichment in the euchromatin regions of myonuclei. In EDL and soleus muscles of WT mice with sciatic nerve transection (SNT), *ANKRD1* expression was quickly elevated post operation, especially in EDL muscles and gradually decreased over time. In contrast, the upregulation of *ALDH3A1* occurred with a multi-day delay in soleus, while no significant upregulation of *ALDH3A1* occurred in EDL muscles even after 14 days. Thus, *ANKRD1* and *ALDH3A1* exhibit inverse induction pattern over muscle type and time post denervation.

To confirm that ALDH3A1 detoxifies reactive aldehydes in muscle, we enforced *ALDH3A1* expression using adeno-associated virus (AAV) vector in myotubes derived from WT EDL or soleus myoblasts. The overexpression of ALDH3A1 markedly decreased 4-HNE induced DNA fragmentation and plasma membrane damage. Furthermore, MG53 is a muscle specific tripartite motif family protein nucleating the assembly of the repair machinery on injured plasma membrane [30]. We previously reported abnormal MG53 intracellular aggregation and compromised membrane repair in ALS muscles [31]. Here we observed sustainable GFP-MG53 signals on the plasma membrane after saponin-induced membrane injury in 86% of GFP-MG53 transfected myotubes. Noticeably, the proportion dropped to 8.6% for myotubes treated with 4-HNE. Importantly, the proportion increased to 77% for myotubes transduced with AAV-ALDH3A1 and treated with 4-HNE. Data here suggest that enforced expression of *ALDH3A1* in cultured myotubes protected against 4-HNE induced DNA fragmentation, plasma membrane damage and restored MG53 mediated membrane repair.

In summary, we elucidated that the muscle type dependent regulation of *ALDH3A1* expression could contribute to variations in muscle resistance to ALS progression due to the protection against reactive aldehyde cytotoxicity. Our discoveries may inspire the development of novel therapeutic measures for muscle degeneration.

Results

Differential expression of *ALDH3A1* across muscles and disease state

We first investigated the transcription levels of the two eye-enriched aldehyde dehydrogenase *ALDH1A1* and *ALDH3A1* in muscles from different anatomic origins, including hindlimb (EDL and soleus), diaphragm and EOMs by qRT-PCR. These muscles were collected from WT mice and their end-stage G93A littermates (4 pairs of male mice and 4 pairs of female mice at 4-5 months of age). As showed in **Figure 1A** left panels and **Figure 1-Source Data 1**, *ALDH3A1* was expressed prominently higher in EOMs than other muscles in WT mice (59-fold of that in EDL, 22-fold of that in soleus and 91 folds of that in diaphragm). Furthermore, notable induction of *ALDH3A1* was detected for soleus (50-fold) and diaphragm (79-fold) from end-stage G93A mice compared to WT counterparts, while the induction was far less pronounced for EDL (7-fold). In G93A EOMs, *ALDH3A1* expression was maintained at comparable levels to WT counterparts. This pathological induction pattern is interesting as EDL is the most severely affected muscle by ALS progression in these four [4, 5]. Importantly, denervation-associated pathological remodeling marker *ANKRD1* (*CARP)* exhibited stronger induction in G93A EDL muscle (69-fold) than diaphragm (35-fold), soleus (22-fold) and EOMs (3-fold) (**Figure 1A** right panels and **Figure 1-Source Data 1**). Data here suggest a potential relationship between *ALDH3A1* expression and muscle resistance to degeneration in ALS. Since

there exist reports of gender-related differences in disease progression in G93A mice [32, 33], we also compared the gene expression levels of *ALDH3A1* and *ANKRD1* in both male and female G93A mice and found no significant differences (**Figure 1-figure supplement 1A**). Data here indicate that female and male G93A mice may share similar extent of pathological remodeling in muscles when disease progresses to the end-stage, while the cross-gender differences could be more apparent at earlier phases such as disease onset.

In contrast to *ALDH3A1*, *ALDH1A1* expression was only marginally different between EOMs and other muscles from WT mice, while no significant difference was detected between EOMs and other muscles from G93A mice. In addition, no significant difference of *ALDH1A1* expression was found when comparing the same type of muscle from WT mice to their G93A counterpart (**Figure 1-figure supplementary 1B** and **Figure 1-Source Data 1**). The data indicate that *ALDH1A1* may not be involved in differential muscle response to ALS progression.

To evaluate whether the unique expression pattern of *ALDH3A1* gene is also present at the protein level, we extracted protein from the four types of muscles from G93A mice and their WT littermates for Western blot. As expected, in WT mice, ALDH3A1 protein was most abundant in EOMs (132-fold of that in EDL, 24-fold of that in soleus and 29-fold of that in diaphragm after normalization to housekeeping protein GAPDH). In line with the qPCR results, the abundance of ALDH3A1 protein was maintained at high levels in EOMs in end-stage G93A mice. Remarkably, significantly elevated levels of ALDH3A1 protein were detected in diaphragm (14-fold), soleus (6-fold) and EDL muscle (5-fold) compared to WT counterparts (**Figure 1B, C, Figure 1-figure supplement 2** and **Figure 1-Source Data 2**). In comparison, ANKRD1 protein increased most significantly in G93A EDL muscle compared to WT counterparts (594-fold), followed by diaphragm (66-fold), soleus (51-fold) (**Figure 1B, C, Figure 1-figure supplement 2** and **Figure 1-Source Data 2**). Consistently, in the transverse section of EDL muscles from G93A mice, most myofibers were positively stained with anti-ANKRD1 antibodies (**Figure 2A**). ANKRD1 positive myofibers were relatively sparse in G93A soleus and diaphragm muscles, while in G93A EOMs they were extremely scarce (1% or less). To further validate the association between ANKRD1 and denervation, we performed sciatic nerve transection (SNT) in the right hindlimbs of WT mice 4-5 months of age. The left hindlimbs were sham operated to serve as controls. The majority of EDL and soleus myofibers were ANKRD1 positive at Day 3 post SNT and the proportion decreased over time (**Figure 2B**).

Thus, our data implied an inverse relationship between *ALDH3A1* expression pattern and that of the denervation marker *ANKRD1* in G93A muscles.

Differential spatial distribution of ALDH3A1 and ANKRD1 protein in myofibers

Next, we did whole-mount immunostaining to investigate the distribution of ALDH3A1 protein in myofibers (**Figure 3A** and **Figure 3-figure supplement 1A**). In WT mice 4-5 months of age, EOM myofibers exhibited higher levels of cytosolic ALDH3A1 than counterparts from other muscles, confirming the Western blot and qPCR data in **Figure 1**. In muscles from end-stage G93A mice, we observed plentiful of myofibers with increased ALDH3A1 in the cytosol and myonuclei in soleus and diaphragm, while these myofibers were scarce in EDL muscles (**Figure 3A** and **Figure 3-figure supplement 1A**, yellow arrows). Upon closer inspections we noticed the dip of nuclear ALDH3A1 signal in the DAPI dense foci, where genomic DNA is highly compacted (**Figure 3B** and **Figure 3-figure supplement 1B**) [34]. Thus, nuclear ALDH3A1 is preferentially localized in the euchromatin regions, a pattern commonly seen for histone modifications associated with actively transcribing genes [35]. Additionally, when we examined the neuromuscular junctions (NMJs) of these myofibers,

we found that axon terminals (labelled by SG2 antibody) were partially or fully absent from AChR positive area (labelled by Alexa Fluor-tagged BTX), indicating that these myofibers were partially or fully denervated. These data further support that the induction of *ALDH3A1* expression is less robust in G93A EDL muscles than in soleus and diaphragm. We speculate that the elevation of ALDH3A1 levels in G93A muscles is a self-defense mechanism protecting cytosolic protein and vulnerable genomic DNA regions against lipid peroxidation stress under ALS.

Next, we compared the spatial distribution of ALDH3A1 and ANKRD1 protein in transverse sections of different muscles from end-stage G93A mice. As demonstrated in **Figure 2A**, most myofibers in G93A EDL muscles were positive for ANKRD1 in the cytosol. But few of these ANKRD1 positive myofibers were also positive for ALDH3A1 (**Figure 4A**, yellow arrows). ANKRD1 positive myofibers were sparser in G93A soleus and diaphragm, whereas myofibers with elevated cytosolic and nuclear ALDH3A1 were more frequently seen (**Figure 4B, C**, yellow arrows). These ALDH3A1 positive myofibers could either be ANKRD1 positive (yellow arrows) or negative (blue arrows) (**Figure 4B, C**). In G93A EOMs, ANKRD1 positive myofibers were extremely scarce, whereas most G93A EOM myofibers exhibited decent levels of cytosolic ALDH3A1 (**Figure 4D**), a feature shared by their WT peers (**Figure 4-figure supplement 1**). In sum, although ALDH3A1 and ANKRD1 are not mutually exclusive in individual myofibers, their abundance does exhibit an inverse relationship on the whole-muscle scale across different muscles in end-stage G93A mice (**Table 1)**.

Table 1. Percentages of ALDH3A1 positive myofibers stained positive or negative for ANKRD1 in different muscles from end-stage G93A mice (N = 6).

G93A Mouse	Gender	Muscle	ANKRD1 positive	ANKRD1 negative
1	F	EDL	100.00	0.00
2	F	EDL	80.00	20.00
3	F	EDL	100.00	0.00
4	M	EDL	100.00	0.00
5	M	EDL	100.00	0.00
6	M	EDL	100.00	0.00
1	F	SOL	45.00	55.00
2	F	SOL	30.00	70.00
3	F	SOL	50.00	50.00
4	M	SOL	71.43	28.57
5	M	SOL	50.00	50.00
6	M	SOL	50.00	50.00
1	F	DIA	84.62	15.38
2	F	DIA	82.35	17.65
3	F	DIA	72.41	27.59
4	M	DIA	70.00	30.00
5	M	DIA	85.11	14.89
6	M	DIA	85.71	14.29
1	F	EOM	1.15	98.85
2	F	EOM	0.00	100.00
3	F	EOM	1.20	98.80
4	M	EOM	0.00	100.00
5	M	EOM	0.87	99.13
6	M	EOM	0.63	99.37

188

189 **Differential temporal profiles of *ALDH3A1* and *ANKRD1* expression in EDL and soleus**
190 **muscles after sciatic nerve transection**

191 To better understand how *ALDH3A1* expression changes in response to denervation, we
192 performed sciatic nerve transection (SNT) in the right hindlimbs of WT mice 4-5 months of age. The
193 left hindlimbs were sham operated to serve as controls. The changes of gene expression in EDL and
194 soleus samples with SNT (compared to their sham-operated controls) were examined at Day 3, Day 7
195 and Day 14 post operation by qRT-PCR (**Figure 5A** and **Figure 5-Source Data 1**). In EDL muscles
196 with SNT, *ALDH3A1* expression was barely changed throughout the two weeks. In soleus with SNT,
197 *ALDH3A1* expression remained comparable to that of sham-operated controls at Day 3 post
198 operation. Yet upregulation was detected at Day 7 and Day 14. This time-dependent change of
199 *ALDH3A1* expression was also confirmed at the protein level by Western blot, with significant
200 elevation detected in soleus but not EDL at Day 7 and Day 14 post SNT (**Figure 5B**, **Figure 5-figure**
201 **supplement 1** and **Figure 5-Source Data 2**). In contrast to *ALDH3A1*, *ANKRD1* expression was
202 elevated in both EDL and soleus at Day 3 post SNT already (**Figure 5A**). Western blot also indicated
203 that ANKRD1 protein levels already peaked at Day 3 post SNT and decreased afterwards (**Figure 5**,
204 **Figure 5-figure supplement 1** and **Figure 5-Source Data 3**). It is worthing noticing that the increase
205 of ANKRD1 protein was more pronounced in EDL (333-fold) compared to soleus (45-fold) at Day 3
206 post SNT, while the increase of ALDH3A1 protein was significant in soleus (7.6-fold) but not in EDL
207 (1.6-fold) at Day 14 post SNT.

208 Through whole-mount immunostaining, we confirmed the complete denervation of myofibers in
209 both EDL and soleus after SNT by the absence of axonal terminals (labelled by SG2 antibody) in
210 NMJs (the AChR-positive area) (**Figure 6A**). Myofibers with nuclear enriched ALDH3A1 was spotted
211 in soleus at Day 7 post SNT. At Day 14 post SNT, we observed more myofibers with increased
212 ALDH3A1, not only in the myonuclei, but also in the cytosol (**Figure 6A**, insets). However, no
213 noticeable increase of ALDH3A1 was observed in EDL myofibers 3-14 days after SNT compared to
214 sham operated controls. Consistently, immunostaining revealed presence of ALDH3A1 positive
215 myofibers in transverse sections of soleus but not EDL muscles at Day 14 post SNT, whereas higher
216 proportions of ANKRD1 positive myofibers were observed in these EDL muscles than soleus (**Figure**
217 **6B**). Date here, together with Figure 2B, further suggest that the induction pattern of *ALDH3A1*
218 expression is inversely related to that of *ANKRD1* over time and muscle type post denervation,
219 although they could be present in the same individual myofiber.

220 **Transducing myotubes with AAV-ALDH3A1 protects against 4-HNE induced apoptosis and**
221 **plasma membrane defects**

222 4-HNE is the most toxic reactive aldehyde generated during lipid peroxidation [36]. To evaluate its
223 cytotoxicity in muscle, EDL and soleus myoblasts derived from WT mice 4-5 months of age were
224 induced to differentiate into myotubes and treated with 0, 7.5, 15 or 30 μM concentrations of 4-HNE
225 for 2 hours. Afterwards myotubes were cultured for another 16 hours in regular differentiation medium
226 before TUNEL staining, as apoptosis can take 12-24 hours to occur [37]. TUNEL positive nuclei
227 (indicative of apoptotic cell death hallmarked by DNA fragmentation) were scarce in myotubes treated
228 with 0, 7.5 or 15 μM 4-HNE but dramatically increased in myotubes treated with 30 μM 4-HNE (53%
229 for myotubes derived from EDL myoblasts, 20% for myotubes derived from soleus myoblasts),
230 accompanied by notable detachment of myotubes from the culture chamber (**Figure 7A, B** and

Figure 7-Source Data 1). Due to the extensive occurrence of myotube detachment, calculating the percentage of TUNEL positive nuclei may not accurately reflect 4-HNE cytotoxicity. Thus, we adopted another cytotoxicity assay based on the leakage of lactate dehydrogenase (LDH) from cytosol, which also revealed a notable uptick of damaged myotubes at 30 μM 4-HNE (65.6% for myotubes derived from EDL myoblasts, 78.4% for myotubes derived from soleus myoblasts. See **Figure 7C** and **Figure 7-Source Data 2**). Intriguingly, AAV-ALDH3A1 transduced myotubes, which had 2 to 6-fold higher levels of ALDH3A1 protein (**Figure 8A** and **Figure 8-Source Data 1**), exhibited dramatically lower percentage of apoptotic nuclei (3.5% for myotubes derived from EDL myoblasts, 0.83% for myotubes derived from soleus myoblasts. See **Figure 8B, C** and **Figure 8-Source Data 2**) and LDH leakage (30.4% for myotubes derived from EDL myoblasts, 38.4% for myotubes derived from soleus myoblasts. See **Figure 8D** and **Figure 8-Source Data 3**). Meanwhile the transduction of AAV-ALDH3A1 alone did not change myotube viability compared to non-transduced controls (**Figure 8D**).

Increased LDH leakage and myotube detachment following 4-HNE treatment indicate compromised plasma membrane integrity. We previously reported defects in MG53 mediated membrane repair mechanism in end-stage G93A mice [31, 38]. Here we move forward to examine the impact of 4-HNE treatment on the formation of stable MG53 repair patches in myotubes with overexpression of GFP-MG53 [30]. Without 4-HNE treatment, GFP-MG53 was predominantly cytosolic and quickly translocated to the plasma membrane in response to saponin (a reagent to trigger MG53 repair patch formation by partially permeabilizing plasma membrane). About 86% recorded myotubes maintained elevated membranous GFP-MG53 signal at the end of recording, implying the formation of stable MG53 repair patches (**Video 1, Figure 9** and **Figure 9-Source Data 1**), while the proportion dropped to 8.6% for myotubes treated with 30 μM 4-HNE for 2 hours before recording (**Figure 9B, D** and **Figure 9-Source Data 1**). A good portion of 4-HNE treated myotubes already had blebs on the plasma membrane before saponin administration. Additionally, the peak intensity of membranous GFP-MG53 signals were also lower than those not treated with 4-HNE (**Figure 9C**). These observations indicate that plasma membrane damage have already occurred during 4-HNE treatment (**Video 2** and **Figure 9**). Intriguingly, pretreatment of myotubes with AAV-ALDH3A1 before 4-HNE treatment not only prevented 4-HNE induced plasma membrane blebbing, restored the peak intensity of membranous GFP-MG53 signal, but also increased the proportion of myotubes maintaining elevated membranous GFP-MG53 signal to 77% (**Video 3**, **Figure 9** and **Figure 9-Source Data 1**).

Discussion

In this study we discovered that ALDH3A1 protein is extremely abundant in mouse EOMs and can be upregulated in other muscles under pathological conditions such as denervation and ALS progression. The extent of *ALDH3A1* upregulation in the ALS mouse model (G93A) vary over muscle type, more prominent in soleus, diaphragm than EDL muscles. In contrast, the muscle pathological remodeling marker *ANKRD1* is more substantially elevated in EDL muscles than soleus and diaphragm of G93A mice. The induction pattern of *ALDH3A1* is also inverse to that of *ANKRD1* over muscle type and time in WT mice with sciatic nerve transection. In addition, the protective effects of ALDH3A1 against 4-HNE in muscle are multi-faceted, from DNA fragmentation in the nuclei to plasma membrane damage and repair defects involving MG53.

ALDH3A1 has been reported to be an inactivation-resistant detoxifier of reactive aldehydes such as 4-HNE in an enzyme kinetics study [23]. Here we detected pronounced increase in nuclear DNA

fragmentation, myotube detachment, LDH leakage, failed formation of MG53 repair patches in myotubes treated with 30 μM 4-HNE for 2 hours, implying that this treatment condition overwhelmed the physiological detoxification capacity. Excitingly, pretreatment of myotubes with AAV-ALDH3A1 potently protected myotubes against all the above cytotoxic effects caused by 4-HNE. In addition, AAV-ALDH3A1 transduction alone did not alter myotube viability as shown by LDH leakage assay, which increases the likelihood for its therapeutic application in the future.

Nuclear enrichment of ALDH3A1 has been observed previously in cultured human and rabbit corneal epithelial cells overexpressing *ALDH3A1* [25, 39, 40]. Since reactive aldehydes such as 4-HNE can directly modify genomic DNA, leading mutagenesis and fragmentation in COS-7 monkey kidney fibroblast-like cells, Chinese hamster ovary (CHO) cells, as well as Swiss 3T3 fibroblasts [16, 21, 22], the DNA protection role of ALDH3A1 has been investigated. Indeed, it was reported to prevent DNA damage and apoptosis induced by 4-HNE, hydrogen peroxide, tert-butyl peroxide, etoposide, mitomycin and UVR in cultured human corneal epithelial (HCE) cells and stromal fibroblasts [20, 39-42]. Aside from its role to directly detoxify reactive aldehydes, ALDH3A1 was also reported to promote a series of DNA damage detection/repair related processes in HCE cells including prolonging cell cycle, increasing levels of total and phospho (Ser15) p53 and activating ATM/ATR signaling pathway, which is central to the maintenance of genome integrity [39, 40, 42-44]. These effects could be a unique advantage of applying ALDH3A1 in therapy. Interestingly, in HCE cells overexpressing *ALDH3A1,* the expression of *GADD45A*, which is also a muscle denervation marker [45], was found to be downregulated [42], indicating the inverse correlation between the expression levels of *ALDH3A1* and muscle denervation marker *ANKRD1* may not be a coincidence, but a phenomenon broadly present in different tissues. In this study, we did kymographic profiling of ALDH3A1 inside myonuclei and unveiled its preferential distribution in the euchromatin regions, where genomic DNA is less compacted and could be more vulnerable to attacks by reactive aldehydes. It is reasonable to hypothesize that *ALDH3A1* upregulation in muscle is a self-defense mechanism against pathologically elevated lipid peroxidation stress not only to protect cytosolic protein but also to maintain genome DNA integrity.

ALDH3A1 expression can be activated through KEAP1-NRF2 signaling [46, 47]. When the binding of KEAP1 to NRF2 is disrupted, NRF2 can escape ubiquitination/degradation and translocate to the nuclei, activating the expression of genes containing electrophile response element (EpRE) in the promoter region [46]. EpRE is present in the 5' upstream region of human *ALDH3A1* gene [47]. The activation of NRF2 signaling has been reported to enhance exercise endurance capacity, augment skeletal muscle regeneration after ischemia-reperfusion injury and ameliorate muscle mass/contractility decline during aging [48-53]. In addition, NRF2 signaling activator edaravone (Radicava) has been approved by FDA to combat ALS [54, 55]. The muscle dependent upregulation of *ALDH3A1* due to ALS progression or chronic denervation we observed here may indicate that the thresholds of NRF2 signaling activation are different among muscles. It is worth further investigation whether the antioxidation effects of NRF2 activators are also different across muscles after systemic administration.

The results of LDH leakage assay for 4-HNE and ALDH3A1 treated myotubes intrigued us to explore their roles in MG53 mediated plasma membrane repair. Previous studies implied cysteine 242 as a redox sensor for mouse MG53 to oligomerize or crosslink [30, 56]. Meanwhile cysteine is the residue most prone to 4-HNE attack through Michael addition [57, 58]. Interestingly, similar to the time-lapse imaging results of 4-HNE treated myotubes expressing GFP-MG53 we reported here,

cardiomyocytes expressing GFP-MG53(C242A), which mutates cysteine 242 to alanine, also demonstrated failed maintenance of membranous signal after the application of saponin [56]. Thus, whether C242 of MG53 is one of the residues forming Michael adducts with 4-HNE in muscles of G93A mice is worth further investigation. The result may explain the abnormal formation of cytosolic MG53 aggregates in these muscles [59].

In sum, we identified multi-faceted benefits of ALDH3A1 against reactive aldehyde cytotoxicity in this study, which encourages us to explore its therapeutic potential for diseases associated with elevated levels of lipid peroxidation in future studies.

Materials and methods

Key Resources Table

Reagent type (species) or resource	Designation	Source or reference	Identifiers	Additional information
Strain, strain background (*Mus musculus*)	B6SJLF1/J	Jackson Laboratory	Stock # 100012	WT mice Both male and female Age up to 4 months
Strain, strain background (*Mus musculus*)	B6SJL-Tg (SOD1*G93A)	Jackson Laboratory	Stock # 002726	G93A mice Both male and female Age up to 4 months
Cell line (*Mus musculus*)	Primary cultured mouse satellite cells	This paper		Isolated from EDL or soleus muscles dissected from 4-month-old WT female mice, enriched by 3 rounds of preplating during culture.
Cell line (*Rattus norvegicus*)	Primary cultured rat spinal motor neurons (RSCMNs)	iXCells	SKU # 10RA-033	Isolated from D16 rat embryo spinal cord; Negative for mycoplasma, bacteria, yeast, and fungi.
Transfected construct (*Mus musculus*)	AAVMYO(9P1)-tMCKp-huALDH3A1.HA-WPRE	Vector Biolabs	SKU # AAV-200734	Adeno-associated virus for muscle-specific expression of human ALHD3A1.

Peptide, recombinant protein	Collagenase II	Worthington	Cat # LS004176	Final concentration 0.26%
Peptide, recombinant protein	Dispase II	Sigma Aldrich	Cat # D46931G	Final concentration 0.24%
Peptide, recombinant protein	Hyaluronidase	Worthington	Cat # LS002592	Final concentration 0.16%
Peptide, recombinant protein	DNase I	Worthington	Cat # LS002139	Final concentration 0.04%
Antibody	Anti-human ALDH3A1 (Rabbit polyclonal IgG)	Proteintech	Cat # 15578-1-AP	IF (1:150) WB (1: 2000)
Antibody	Anti-chicken MHC (Mouse monoclonal IgG2b)	Developmental Studies Hybridoma Bank	Cat # MF20	IF (1:200)
Antibody	Anti-rat ANKRD1 (Mouse monoclonal IgG1)	Sigma Aldrich	Cat # MABS1228	IF (1:300) WB (1: 2000)
Antibody	Anti-human GAPDH (Mouse monoclonal IgG2b)	Proteintech	Cat # 60004-1-Ig	WB (1:5000)
Antibody	HRP-conjugated affinipure goat anti-mouse IgG(H+L)	Proteintech	Cat # SA00001-1	WB (1:5000)
Antibody	HRP-conjugated affinipure goat anti-rabbit IgG(H+L)	Proteintech	Cat # SA00001-2	WB (1:5000)
Antibody	Anti-zebrafish Synaptotagmin 2 (Mouse monoclonal	Developmental Studies Hybridoma Bank	Cat # znp-1	IF (1:150)

	IgG2a)			
Recombinant DNA reagent	GFP-MG53	Laboratory of Dr. Jianjie Ma		
Sequence-based reagent	qPCR primers for mouse *ALDH1A1*	Sigma Aldrich		Fwd: GGAATACCGTGGTTGTCAAGCC Rev: CCAGGGACAATGTTTACCACGC
Sequence-based reagent	qPCR primers for mouse *ALDH3A1*	Sigma Aldrich		Fwd: GGTCCTTGTCATAGGTGCTTGG Rev: GAAAGCAGGTCTGCCATGTGATC
Sequence-based reagent	qPCR primers for mouse *ANKRD1*	Sigma Aldrich		Fwd: GCTTAGAAGGACACTTGGCGATC Rev: GACATCTGCGTTTCCTCCACGA
Commercial assay or kit	CF640R TUNEL Assay Apoptosis Detection Kit	Biotium	Cat # 30074	1.5 hours incubation with the reaction mix containing TdT
Commercial assay or kit	Direct-zol RNA MiniPrep Plus	Zymo Research	Cat # R2070	
Commercial assay or kit	GoScript Reverse Transcriptase Mix + Oligo(dT)	Promega	Cat # A2791	
Commercial assay or kit	Universal SYBR Green Fast qPCR Mix	Abclonal	Cat # RK21203	
Commercial assay or kit	CytoTox 96 Non-Radioactive Cytotoxicity Assay	Promega	Cat # G1780	
Chemical compound, drug	AF 488 conjugated α-	Thermo Fisher Scientific	Cat # B13422	IF (1:1000)

	Bungarotoxin			
Chemical compound, drug	DAPI in water	Biotium	Cat # 40043	IF (1:10000)
Chemical compound, drug	TransfeX transfection reagent	ATCC	Cat #ACS-4005	
Chemical compound, drug	4-HNE	Cayman Chemical	Cat #32100	
Chemical compound, drug	Saponin	Thermo Scientific	Cat #A18820.14	Final concentration 0.00375%
Chemical compound, drug	EGTA	Sigma Aldrich	Cat #E4378	
Chemical compound, drug	BTS	Sigma Aldrich	Cat #203895	

Animals

All animal experiments were carried out in accordance with the recommendations in the *Guide for the Care and Use of Laboratory Animals* of the National Institutes of Health. The protocol on the usage of mice was approved by the Institutional Animal Care and Use Committee of the University of Texas at Arlington (A19.001, approval date: 09/20/2018). WT mice used in this study were of B6SJL background. The ALS transgenic mouse model (hSOD1G93A) with genetic background of B6SJL was originally generated by Drs. Deng and Siddique's group at Northwestern University and deposited to the Jackson Lab as B6SJL-Tg (SOD1*G93A) [27]. G93A mice of both genders were euthanized for sample collection at the endpoint when they were unable to right themselves to a sternal position within 30 seconds (4-5 months of age). WT mice of the corresponding gender were euthanized for sample collection at the same day as their G93A littermates.

Sciatic nerve transection

Surgical instruments were sterilized by autoclave before operation. Mice were anesthetized with constant flow isoflurane inhalation. Hairs in the two posterior thighs and lower back were shaved as much as possible with electric clipper. The skin region to be operated on were aseptically prepared using surgical scrub with betadine or equivalent surgical soap and rinse with 70% alcohol. Incision through the skin and superficial muscles was made parallel and just inferior to the femur of the right hindlimb. Curved-end forceps were used to divide the muscles and expose the sciatic nerve. 5 mm of the sciatic nerve was removed with fine surgical scissors. Both ends of the nerve were sutured to prevent regeneration. The incision on the skin was closed with stainless steel wound clips. A sham

procedure following the same steps without severing the sciatic nerve was performed for the left hindlimb as control.

Immunofluorescence (IF) and imaging of whole mount and muscle samples

For whole mount immunofluorescence, EDL, soleus, diaphragm and EOM samples were fixed and permeabilized in precooled methanol at -20 °C for 15 min. The samples were rehydrated by three changes of PBS and incubated with Alexa Fluor 488 conjugated α-Bungarotoxin (Thermo Fisher B13422, 1:1000) in blocking buffer (PBS containing 2% BSA, 2% horse serum, 0.1% Tween-20, 0.1% Triton X-100 and 0.05% sodium azide) at 4 °C for 1 day. The samples were then washed with PBS and further incubated with the primary antibodies against ALDH3A1 (Proteintech 15578-1-AP 1:150) and Synaptotagmin-2 (SG2 for short, DSHB ZNP-1 concentrate + 50% glycerol 1:150) in blocking buffer at 4 °C for 1 day. On the third day, the samples were washed with PBS for 3 times and incubated with corresponding secondary antibodies labelled with Alexa Fluor.

For section immunofluorescence, EDL, soleus, diaphragm and EOM were fixed in 3% glyoxal fixative (pH 4.5, containing 20% ethanol) for 8-12 hours at 4 °C. We chose glyoxal over paraformaldehyde because of the faster tissue penetration rate and avoidance of protein crosslinking [60-62]. Antigen retrieval was conducted in Tris-EDTA buffer (pH 9.0) for 30 min at 95 °C. Afterwards the samples were washed with PBS containing 1% glycine once and two more times with PBS. Then the samples were immersed in blocking buffer for 45 min at room temperature followed by primary antibody incubation at 4 °C overnight. Next day, after washing with PBS for three times, the samples were incubated with Alexa Fluor labelled secondary antibodies (Thermo Fisher 1:800) for 2 hours at room temperature. The samples were then washed with PBS, counterstained with DAPI and mounted in antifade mounting media (20 mM Tris, 0.5% N-propyl gallate, 80% glycerol) for imaging. Primary antibodies used: ALDH3A1, ANKRD1 (Sigma MABS1228 1:200)

RNA extraction and qRT-PCR

Homogenization was performed in FastPrep-24 Classic bead beating grinder (MP Biomedicals 116004500). The tissue homogenate was transfer to centrifuge tubes containing phase lock gel (QuantaBio 2302830) and 1/10 volume of 1- bromo-3-chloropropane was added. The tubes were hand shaken for 12 seconds, left at bench top for 2 minutes and then centrifuged at 16000 g at 4 °C for 15 minutes. The upper phase was transferred to a new centrifuge tube and mixed with equal volume of ethanol. The following steps of RNA purification was performed with Direct-zol RNA Miniprep Plus kit (Zymo Research R2070). RNA concentration was measured with Quantus Fluorometer (Promega E6150). GoScript Reverse Transcription Mix, oligo(dT) was used for the reverse transcription reaction (Promega A2791). First-strand cDNAs were diluted and mixed with 2X Universal SYBR Green Fast qPCR Mix (Abclonal RK21203), as well as corresponding primers for qPCR using StepOnePlus Real-Time PCR system (Thermo Fisher 4376600). Relative quantification (RQ) of gene expression was generated by ΔΔCt method. The sequences of primers used for qPCR were listed in Key Resource Table.

Western blot

Proteins were extracted by grinding corresponding muscles in 10 volumes of RIPA buffer containing protease inhibitors (Thermo Fisher Scientific), resolved by SDS-PAGE, and transferred to PVDF membrane with Bio-Rad semidry transfer cell. The primary antibodies were ALDH3A1 (Proteintech 15578-1-AP), ANKRD1 (Sigma MABS1228) and GAPDH (Proteintech 60004-1-Ig).

Protein bands were detected with Bio-Rad Clarity ECL kit and ChemiDoc Imaging system. Signal strengths and backgrounds were measured using ImageJ software.

Primary culture of myoblasts

EDL or soleus muscles were dissected from two 4-month-old WT female mice and placed in 0 mM Ca^{2+} Ringer's solution. Excessive connective tissue, tendons, fat, blood clots and vessels were removed as much as possible. After cleanup, the muscles were transferred into the digestion media (DMEM containing 5% FBS, 1% Pen/Strep and 10 mM HEPES) and minced into small blocks using scissors. Collagenase II (Worthington LS004176, ≥125 units/mg), dispase II (Sigma D46931G, ≥0.5 units/mg), hyaluronidase (Worthington LS002592, ≥300 USP/NF units/mg) and Dnase I (Worthington LS002139, ≥2,000 Kunitz units/mg) were added at the final concentration of 0.26%, 0.24%, 0.16% and 0.04% (weight/volume), respectively. The digestion system was placed in an orbital shaker running at 70 rpm at 37 °C for 45 min. The digested muscles were triturated 10 times with a 20-gauge needle attached to a 5 ml syringe. Afterwards the triturated mixture was pipetted onto a pre-wetted 100 μm strainer and centrifuge at 100 g for 2.5 min to precipitate the bulky myofiber debris. The supernatant was transferred onto a pre-wetted 40 um strainer and cells were collected by centrifuged at 1200 g for 6.5 min. After the removal of supernatant, cells were resuspended with 5 ml growth medium (Ham's F-10 medium + 20% FBS + 1%Pen/Strep + 5ng/ml bFGF + 10 μg/ml Plasmocin and pre-plated in non-coated T25 flasks at 37 °C for 30 min. The unattached cells were transferred together with medium to Matrigel coated T25 flasks and cultured till reaching about 50% confluence. Pre-plating continued for three more passages to diminish non-myoblast cells.

4-HNE and AAV treatment

Cultured myoblasts derived from soleus or EDL muscles of 4-month-old WT mice (seeded in laminin coated chambered cover glass at about 2.5x10^4/compartment) were induced to differentiate into myotubes in low serum medium (DMEM+2% horse serum) for four days, with medium changed every other day. 4-HNE treatment was performed at 0, 7.5, 15, 30 μM for 2 hours. The treatment time was determined based on a previous study showing 4-HNE notably induced oxidative stress as early as 2 hours in Swiss 3T3 fibroblasts [22].

AAVMYO(9P1)-tMCKp-huALDH3A1.HA-WPRE (AAV-ALDH3A1 for short) was produced by Vector Biolabs. AAVMYO(9P1) is a mutant of AAV9 that shows superior efficiency and specificity in skeletal and cardiac muscles [63]. The triple muscle creatine kinase promoter (tMCKp) specifically drives gene expression in differentiated muscle tissue [64]. To carry out AAV transduction, cultured myoblasts derived from soleus or EDL muscles of WT mice 4-5 months of age (seeded in laminin coated 48-well plate or chambered cover glass at about 2.5x10^4/compartment) were induced to differentiate into myotubes with low serum medium containing AAV-ALDH3A1 (1x10^11 GC/ml) for 2 days and regular differentiation medium for another 2 days. 4-HNE treatment (30 μM for 2 hours) was performed at the end of the second day. After the transient exposure to 4-HNE, myotubes were cultured for another 16 hours in regular low serum medium before TUNEL assay (Biotium 30074) or LDH leakage-based cytotoxicity assay (Promega G1780). This is because apoptosis can take 12-24 hours to occur [37].

TUNEL assay

Triplicate cultures of myotubes in chambered cover glass (Cellvis C8-1.5H-N) were fixed and permeabilized with precooled methanol at -20 °C for 15 min. Afterwards, the samples were

rehydrated by washing with PBS for 3 times (5 min each). TUNEL staining was performed following the manual of Biotum CF640R TUNEL Assay Apoptosis Detection Kit. The incubation time with the reaction mix (containing TdT enzyme) was 1.5 hours at 37 °C. Afterwards, the samples were washed twice with PBS and incubated with blocking buffer for 45 min at room temperature, followed by immunostaining with ALDH3A1 and myosin heavy chain (DSHB, MF-20 1:100) antibodies. Counterstaining with DAPI was done to calculate the ratio of nuclei with fragmented genomic DNA.

Non-radioactive cytotoxicity (LDH leakage) assay

We generally followed the protocol of the assay kit (Promega, G1780). In brief, 5-6 replicates of myotube cultures with or without AAV transduction, 4-HNE treatment, were cultured in 300 µl regular low serum medium for 16 hours, along with wells containing only 300 µl medium but no cells (to serve as medium only controls and volume correction controls). Next morning, 50 µl of culture supernatant was collected and 50 µl of lysis solution (contains Triton X-100) was added to lyse all the remaining myotubes (37 °C, 45 min). The supernatant, the medium only control, the all-cell-lysed solution (12.5 µl diluted to 50 µl with PBS+1% BSA, 1:4 dilution) and the volume correction controls (medium only wells with 50 µl replaced with lysis solution and diluted 1:4 with PBS+1% BSA) were combined with 50 µl of chromogenic substrates of lactate dehydrogenase (LDH, a stable cytosolic enzyme that is released upon cell death), respectively, for absorbance measurement by a plate reader (SpectraMax i3x, Molecular Devices). Absorbance at 490 nm was recorded every 5 min for 35 min for each sample. The largest rate of absorbance increase (Vmax) calculated from 3 continuous points out of the 7 time points measured reflects the concentration of LDH. To compare the percentages of dead myotubes under different treatment conditions, we calculated the percentage of LDH in the culture supernatant to total LDH as follows: 100*(Vmax(supernatant)-Vmax(medium only control))/(4*(Vmax(all-cell-lysed)-Vmax(volume correction control))+(Vmax(supernatant)-Vmax(medium only control))/6).

Transfection of GFP-MG53 and recording of saponin induced MG53 membrane translocation

4.5x10^4 of myoblasts derived from soleus muscles of 4-month-old WT mice were seeded into glass bottom dishes (Matsunami D35-14-1.5-U) and cultured in growth medium overnight before transfection of 3 µg GFP-MG53 plasmids with TransfeX transfection reagent (ATCC ACS-4005). We selected soleus derived myoblasts because they form multi-nuclei, lengthy myotubes more robustly than EDL derived ones, facilitating the measurement of membranous GFP-MG53 signals.GFP-MG53 was a gift from Dr. Jianjie Ma's lab [30]. One day after transfection, the culture medium was changed to low serum medium to induce differentiation for 4 days, with medium changed every two days. AAV-ALDH3A1 treatment group was incubated with the AAV vector at the first two days of differentiation. 4-HNE treatment group was incubated with 30 µM 4-HNE for 2 hours at the end of the 4-day differentiation. The myotubes were washed three times with 0 mM Ca^{2+} Ringer's solution containing 0.5 mM EGTA (Sigma Aldrich E4378) and 90 µM BTS (Sigma Aldrich 203895) to prevent contraction. Time lapse imaging of myotubes were performed with Leica TCS SP8 confocal microscope at an interval of 2 sec for 3 min. 0.00375% saponin (Thermo Scientific A18820.14) was applied 10 sec after recording started. Regions of interest were generated at plasma membrane regions and background signals from myotube free area was deduced to acquire GFP-MG53 intensity profile (F) over time. F_0 was the averaged intensity of the first 4 frames.

Data analysis and statistics

Box-and-dot plots were generated with ggplot2 package of R. The lower hinge, median line and upper hinge correspond to the first, second and third quartiles. The lower and upper whiskers extend

from the hinges to the largest value no further than 1.5 times of inter-quartile range (distance between the first and third quartiles). Data beyond the end of the whiskers are outlying points. Wilcoxon rank-sum tests were used to compare means of two groups unless there were tie values between two groups (**Figure 7B**) or the group had less than 4 samples (**Figure 8A**). In those cases, t.test was used instead. For multi-group data, one-way ANOVA P values were generated by aov function of R.

Acknowledgement: We thank Dr. Yongfu Wang at and Dr. Ji Pang, who previously worked at Stowers Institute for Medical Research, for the help in trouble-shooting the glyoxal fixation protocol for section immunofluorescence.

Funding: This study has been supported by grants from NIH (R01NS105621 to JZ, R01NS129219 to JZ and JM) and the Department of Defense AL170061(W81XWH1810684) to JZ.

Author contributions

Ang Li, Conceptualization, Data curation, Formal analysis, Validation, Investigation, Visualization, Methodology, Writing – original draft, Project administration, Writing – review and editing; Li Dong, Xuejun Li, Jianxun Yi, Data curation, Validation, Investigation, Methodology; Jianjie Ma, Conceptualization, Funding acquisition, Writing – review and editing; Jingsong Zhou, Conceptualization, Resources, Supervision, Funding acquisition, Validation, Investigation, Visualization, Methodology, Writing – original draft, Project administration, Writing – review and editing

References

1. Domellöf, F.P. (2019). The Extraocular Muscles Are Selectively Spared in ALS. In Amyotrophic Lateral Sclerosis-Recent Advances and Therapeutic Challenges. (IntechOpen).
2. Tjust, A.E., Brännstrom, T., and Pedrosa Domellöf, F. (2012). Unaffected motor endplate occupancy in eye muscles of ALS G93A mouse model. Frontiers in bioscience (Scholar edition) *4*, 1547-1555.
3. Ahmadi, M., Liu, J.-X., Brännström, T., Andersen, P.M., Stål, P., and Pedrosa-Domellöf, F. (2010). Human extraocular muscles in ALS. Investigative ophthalmology & visual science *51*, 3494-3501.
4. Valdez, G., Tapia, J.C., Lichtman, J.W., Fox, M.A., and Sanes, J.R. (2012). Shared resistance to aging and ALS in neuromuscular junctions of specific muscles. PloS one *7*, e34640.
5. Li, A., Yi, J., Li, X., Dong, L., Ostrow, L.W., Ma, J., and Zhou, J. (2024). Distinct transcriptomic profile of satellite cells contributes to preservation of neuromuscular junctions in extraocular muscles of ALS mice. Elife *12*, RP92644.
6. Derave, W., Van Den Bosch, L., Lemmens, G., Eijnde, B.O., Robberecht, W., and Hespel, P. (2003). Skeletal muscle properties in a transgenic mouse model for amyotrophic lateral sclerosis: effects of creatine treatment. Neurobiology of disease *13*, 264-272.
7. Chiu, A.Y., Zhai, P., Dal Canto, M.C., Peters, T.M., Kwon, Y.W., Prattis, S.M., and Gurney, M.E. (1995). Age-dependent penetrance of disease in a transgenic mouse model of familial amyotrophic lateral sclerosis. Molecular and Cellular Neuroscience *6*, 349-362.
8. Frey, D., Schneider, C., Xu, L., Borg, J., Spooren, W., and Caroni, P. (2000). Early and selective loss of neuromuscular synapse subtypes with low sprouting competence in motoneuron diseases. J Neurosci *20*, 2534-2542.

9. Di Domenico, F., Tramutola, A., and Butterfield, D.A. (2017). Role of 4-hydroxy-2-nonenal (HNE) in the pathogenesis of alzheimer disease and other selected age-related neurodegenerative disorders. Free Radical Biology and Medicine *111*, 253-261.
10. Li, Y., Zhao, T., Li, J., Xia, M., Li, Y., Wang, X., Liu, C., Zheng, T., Chen, R., and Kan, D. (2022). Oxidative Stress and 4-hydroxy-2-nonenal (4-HNE): Implications in the Pathogenesis and Treatment of Aging-related Diseases. Journal of Immunology Research *2022*.
11. Guéraud, F., Atalay, M., Bresgen, N., Cipak, A., Eckl, P., Huc, L., Jouanin, I., Siems, W., and Uchida, K. (2010). Chemistry and biochemistry of lipid peroxidation products. Free radical research *44*, 1098-1124.
12. Mol, M., Regazzoni, L., Altomare, A., Degani, G., Carini, M., Vistoli, G., and Aldini, G. (2017). Enzymatic and non-enzymatic detoxification of 4-hydroxynonenal: Methodological aspects and biological consequences. Free Radical Biology and Medicine *111*, 328-344.
13. Cai, J., Bhatnagar, A., and Pierce Jr, W.M. (2009). Protein modification by acrolein: formation and stability of cysteine adducts. Chemical research in toxicology *22*, 708-716.
14. Aubourg, S.P. (1993). Interaction of malondialdehyde with biological molecules—new trends about reactivity and significance. International journal of food science & technology *28*, 323-335.
15. Esterbauer, H. (1993). Cytotoxicity and genotoxicity of lipid-oxidation products. The American journal of clinical nutrition *57*, S779-S786.
16. Voulgaridou, G.-P., Anestopoulos, I., Franco, R., Panayiotidis, M.I., and Pappa, A. (2011). DNA damage induced by endogenous aldehydes: current state of knowledge. Mutation Research/Fundamental and Molecular Mechanisms of Mutagenesis *711*, 13-27.
17. Falletti, O., and Douki, T. (2008). Low glutathione level favors formation of DNA adducts to 4-hydroxy-2 (E)-nonenal, a major lipid peroxidation product. Chemical research in toxicology *21*, 2097-2105.
18. Wang, H.-T., Zhang, S., Hu, Y., and Tang, M.-s. (2009). Mutagenicity and sequence specificity of acrolein-DNA adducts. Chemical research in toxicology *22*, 511-517.
19. Liu, X.-y., Zhu, M.-x., and Xie, J.-p. (2010). Mutagenicity of acrolein and acrolein-induced DNA adducts. Toxicology mechanisms and methods *20*, 36-44.
20. Pappa, A., Chen, C., Koutalos, Y., Townsend, A.J., and Vasiliou, V. (2003). Aldh3a1 protects human corneal epithelial cells from ultraviolet-and 4-hydroxy-2-nonenal-induced oxidative damage. Free Radical Biology and Medicine *34*, 1178-1189.
21. Brambilla, G., Sciaba, L., Faggin, P., Maura, A., Marinari, U., Ferro, M., and Esterbauer, H. (1986). Cytotoxicity, DNA fragmentation and sister-chromatid exchange in Chinese hamster ovary cells exposed to the lipid peroxidation product 4-hydroxynonenal and homologous aldehydes. Mutation Research/Genetic Toxicology *171*, 169-176.
22. Kutuk, O., Adli, M., Poli, G., and Basaga, H. (2004). Resveratrol protects against 4‐HNE induced oxidative stress and apoptosis in Swiss 3T3 fibroblasts. Biofactors *20*, 1-10.
23. Yoval-Sánchez, B., and Rodríguez-Zavala, J.S. (2012). Differences in susceptibility to inactivation of human aldehyde dehydrogenases by lipid peroxidation byproducts. Chemical research in toxicology *25*, 722-729.
24. Stewart, M., Malek, K., and Crabb, D.W. (1996). Distribution of messenger RNAs for aldehyde dehydrogenase 1, aldehyde dehydrogenase 2, and aldehyde dehydrogenase 5 in human tissues. Journal of investigative medicine: the official publication of the American Federation for Clinical Research *44*, 42-46.
25. Stagos, D., Chen, Y., Cantore, M., Jester, J.V., and Vasiliou, V. (2010). Corneal aldehyde dehydrogenases: multiple functions and novel nuclear localization. Brain research bulletin *81*, 211-218.
26. Lassen, N., Bateman, J.B., Estey, T., Kuszak, J.R., Nees, D.W., Piatigorsky, J., Duester, G., Day, B.J., Huang, J., and Hines, L.M. (2007). Multiple and additive functions of ALDH3A1 and ALDH1A1: cataract

phenotype and ocular oxidative damage in Aldh3a1 (-/-)/Aldh1a1 (-/-) knock-out mice. Journal of Biological Chemistry *282*, 25668-25676.

27. Gurney, M.E., Pu, H., Chiu, A.Y., Dal Canto, M.C., Polchow, C.Y., Alexander, D.D., Caliendo, J., Hentati, A., Kwon, Y.W., and Deng, H.-X. (1994). Motor neuron degeneration in mice that express a human Cu, Zn superoxide dismutase mutation. Science *264*, 1772-1775.
28. Laure, L., Suel, L., Roudaut, C., Bourg, N., Ouali, A., Bartoli, M., Richard, I., and Danièle, N. (2009). Cardiac ankyrin repeat protein is a marker of skeletal muscle pathological remodelling. The FEBS journal *276*, 669-684.
29. Nakamura, K., Nakada, C., Takeuchi, K., Osaki, M., Shomori, K., Kato, S., Ohama, E., Sato, K., Fukayama, M., and Mori, S. (2003). Altered expression of cardiac ankyrin repeat protein and its homologue, ankyrin repeat protein with PEST and proline-rich region, in atrophic muscles in amyotrophic lateral sclerosis. Pathobiology *70*, 197-203.
30. Cai, C., Masumiya, H., Weisleder, N., Matsuda, N., Nishi, M., Hwang, M., Ko, J.-K., Lin, P., Thornton, A., and Zhao, X. (2009). MG53 nucleates assembly of cell membrane repair machinery. Nature cell biology *11*, 56-64.
31. Yi, J., Li, A., Li, X., Park, K., Zhou, X., Yi, F., Xiao, Y., Yoon, D., Tan, T., and Ostrow, L.W. (2021). MG53 preserves neuromuscular junction integrity and alleviates ALS disease progression. Antioxidants *10*, 1522.
32. Pfohl, S.R., Halicek, M.T., and Mitchell, C.S. (2015). Characterization of the contribution of genetic background and gender to disease progression in the SOD1 G93A mouse model of amyotrophic lateral sclerosis: a meta-analysis. Journal of neuromuscular diseases *2*, 137-150.
33. Alves, C.J., De Santana, L.P., Dos Santos, A.J.D., De Oliveira, G.P., Duobles, T., Scorisa, J.M., Martins, R.S., Maximino, J.R., and Chadi, G. (2011). Early motor and electrophysiological changes in transgenic mouse model of amyotrophic lateral sclerosis and gender differences on clinical outcome. Brain research *1394*, 90-104.
34. Imai, R., Nozaki, T., Tani, T., Kaizu, K., Hibino, K., Ide, S., Tamura, S., Takahashi, K., Shribak, M., and Maeshima, K. (2017). Density imaging of heterochromatin in live cells using orientation-independent-DIC microscopy. Molecular biology of the cell *28*, 3349-3359.
35. Alvarenga, E.M., Rodrigues, V.L., Moraes, A.S., Naves, L.S., Mondin, M., Felisbino, M.B., and Mello, M.L.S. (2016). Histone epigenetic marks in heterochromatin and euchromatin of the Chagas' disease vector, Triatoma infestans. Acta histochemica *118*, 401-412.
36. Esterbauer, H., Schaur, R.J., and Zollner, H. (1991). Chemistry and biochemistry of 4-hydroxynonenal, malonaldehyde and related aldehydes. Free radical Biology and medicine *11*, 81-128.
37. Saraste, A. (1999). Morphologic criteria and detection of apoptosis. Herz *24*, 189.
38. Li, A., Yi, J., Li, X., Dong, L., Ostrow, L.W., Ma, J., and Zhou, J. (2022). Deficient Sarcolemma Repair in ALS: A Novel Mechanism with Therapeutic Potential. Cells *11*, 3263.
39. Pappa, A., Brown, D., Koutalos, Y., DeGregori, J., White, C., and Vasiliou, V. (2005). Human aldehyde dehydrogenase 3A1 inhibits proliferation and promotes survival of human corneal epithelial cells. Journal of Biological Chemistry *280*, 27998-28006.
40. Voulgaridou, G.-P., Theologidis, V., Venetikidou, M., Tsochantaridis, I., Tsolou, A., Koffa, M., Panayiotidis, M.I., and Pappa, A. (2023). Investigating the functional roles of aldehyde dehydrogenase 3A1 in human corneal epithelial cells. International Journal of Molecular Sciences *24*, 5845.
41. Lassen, N., Pappa, A., Black, W.J., Jester, J.V., Day, B.J., Min, E., and Vasiliou, V. (2006). Antioxidant function of corneal ALDH3A1 in cultured stromal fibroblasts. Free Radical Biology and Medicine *41*, 1459-1469.
42. Voulgaridou, G.-P., Tsochantaridis, I., Tolkas, C., Franco, R., Giatromanolaki, A., Panayiotidis, M.I., and Pappa, A. (2020). Aldehyde dehydrogenase 3A1 confers oxidative stress resistance accompanied by

altered DNA damage response in human corneal epithelial cells. Free Radical Biology and Medicine *150*, 66-74.

43. Canman, C.E., Lim, D.-S., Cimprich, K.A., Taya, Y., Tamai, K., Sakaguchi, K., Appella, E., Kastan, M.B., and Siliciano, J.D. (1998). Activation of the ATM kinase by ionizing radiation and phosphorylation of p53. Science *281*, 1677-1679.
44. Awasthi, P., Foiani, M., and Kumar, A. (2015). ATM and ATR signaling at a glance. Journal of cell science *128*, 4255-4262.
45. Bongers, K.S., Fox, D.K., Ebert, S.M., Kunkel, S.D., Dyle, M.C., Bullard, S.A., Dierdorff, J.M., and Adams, C.M. (2013). Skeletal muscle denervation causes skeletal muscle atrophy through a pathway that involves both Gadd45a and HDAC4. Am J Physiol Endocrinol Metab *305*, E907-915.
46. Baird, L., and Yamamoto, M. (2020). The Molecular Mechanisms Regulating the KEAP1-NRF2 Pathway. Mol Cell Biol *40*.
47. Sreerama, L., and Sládek, N.E. (2001). Three different stable human breast adenocarcinoma sublines that overexpress ALDH3A1 and certain other enzymes, apparently as a consequence of constitutively upregulated gene transcription mediated by transactivated EpREs (electrophile responsive elements) present in the 5′ -upstream regions of these genes. Chemico-Biological Interactions *130*, 247-260.
48. Onoki, T., Izumi, Y., Takahashi, M., Murakami, S., Matsumaru, D., Ohta, N., Wati, S.M., Hatanaka, N., Katsuoka, F., and Okutsu, M. (2021). Skeletal muscle-specific Keap1 disruption modulates fatty acid utilization and enhances exercise capacity in female mice. Redox Biology *43*, 101966.
49. Wang, L., Yang, S., Yan, L., Wei, H., Wang, J., Yu, S., Kong, A.-N.T., and Zhang, Y. (2019). Hypoxia preconditioning promotes endurance exercise capacity of mice by activating skeletal muscle Nrf2. Journal of Applied Physiology *127*, 1267-1277.
50. Al‐Sawaf, O., Fragoulis, A., Rosen, C., Keimes, N., Liehn, E.A., Hölzle, F., Kan, Y.W., Pufe, T., Sönmez, T.T., and Wruck, C.J. (2014). Nrf2 augments skeletal muscle regeneration after ischaemia–reperfusion injury. The Journal of pathology *234*, 538-547.
51. Shelar, S.B., Narasimhan, M., Shanmugam, G., Litovsky, S.H., Gounder, S.S., Karan, G., Arulvasu, C., Kensler, T.W., Hoidal, J.R., and Darley-Usmar, V.M. (2016). Disruption of nuclear factor (erythroid-derived-2)–like 2 antioxidant signaling: a mechanism for impaired activation of stem cells and delayed regeneration of skeletal muscle. The FASEB Journal *30*, 1865.
52. Huang, D.-D., Yan, X.-L., Fan, S.-D., Chen, X.-Y., Yan, J.-Y., Dong, Q.-T., Chen, W.-Z., Liu, N.-X., Chen, X.-L., and Yu, Z. (2020). Nrf2 deficiency promotes the increasing trend of autophagy during aging in skeletal muscle: a potential mechanism for the development of sarcopenia. Aging (Albany NY) *12*, 5977.
53. Ahn, B., Pharaoh, G., Premkumar, P., Huseman, K., Ranjit, R., Kinter, M., Szweda, L., Kiss, T., Fulop, G., and Tarantini, S. (2018). Nrf2 deficiency exacerbates age-related contractile dysfunction and loss of skeletal muscle mass. Redox biology *17*, 47-58.
54. Jiménez-Villegas, J., Ferraiuolo, L., Mead, R., Shaw, P., Cuadrado, A., and Rojo, A.I. (2021). NRF2 as a therapeutic opportunity to impact in the molecular roadmap of ALS. Free Radical Biology and Medicine *173*, 125-141.
55. Nightingale, B. (2020). The effect of edaravone on amyotrophic lateral sclerosis. Journal of Neurology Research *10*, 150-159.
56. Wang, X., Xie, W., Zhang, Y., Lin, P., Han, L., Han, P., Wang, Y., Chen, Z., Ji, G., and Zheng, M. (2010). Cardioprotection of ischemia/reperfusion injury by cholesterol-dependent MG53-mediated membrane repair. Circulation research *107*, 76-83.
57. Milkovic, L., Zarkovic, N., Marusic, Z., Zarkovic, K., and Jaganjac, M. (2023). The 4-Hydroxynonenal–Protein Adducts and Their Biological Relevance: Are Some Proteins Preferred Targets? Antioxidants *12*, 856.
58. Dalleau, S., Baradat, M., Guéraud, F., and Huc, L. (2013). Cell death and diseases related to oxidative stress: 4-hydroxynonenal (HNE) in the balance. Cell Death & Differentiation *20*, 1615-1630.

59. Yi, J., Li, A., Li, X., Park, K., Zhou, X., Yi, F., Xiao, Y., Yoon, D., Tan, T., Ostrow, L.W., et al. (2021). MG53 Preserves Neuromuscular Junction Integrity and Alleviates ALS Disease Progression. Antioxidants (Basel) *10*.
60. Richter, K.N., Revelo, N.H., Seitz, K.J., Helm, M.S., Sarkar, D., Saleeb, R.S., d'Este, E., Eberle, J., Wagner, E., and Vogl, C. (2018). Glyoxal as an alternative fixative to formaldehyde in immunostaining and super‐resolution microscopy. The EMBO journal *37*, 139-159.
61. Dapson, R. (2007). Glyoxal fixation: how it works and why it only occasionally needs antigen retrieval. Biotechnic & Histochemistry *82*, 161-166.
62. Pang, J., Zhao, X., Deng, F., Tsuchiya, D., Malloy, S., Parmely, T., Xie, T., and Wang, Y. (2022). A freeze-substitution approach with solvent-based glyoxal fixative to prevent distortion of ocular structures. Journal of Histotechnology *45*, 172-181.
63. Weinmann, J., Weis, S., Sippel, J., Tulalamba, W., Remes, A., El Andari, J., Herrmann, A.-K., Pham, Q.H., Borowski, C., and Hille, S. (2020). Identification of a myotropic AAV by massively parallel in vivo evaluation of barcoded capsid variants. Nature communications *11*, 5432.
64. Wang, B., Li, J., Fu, F., Chen, C., Zhu, X., Zhou, L., Jiang, X., and Xiao, X. (2008). Construction and analysis of compact muscle-specific promoters for AAV vectors. Gene therapy *15*, 1489-1499.

698

699

700

701

702

703 **Figure and figure legends**

Figure 1

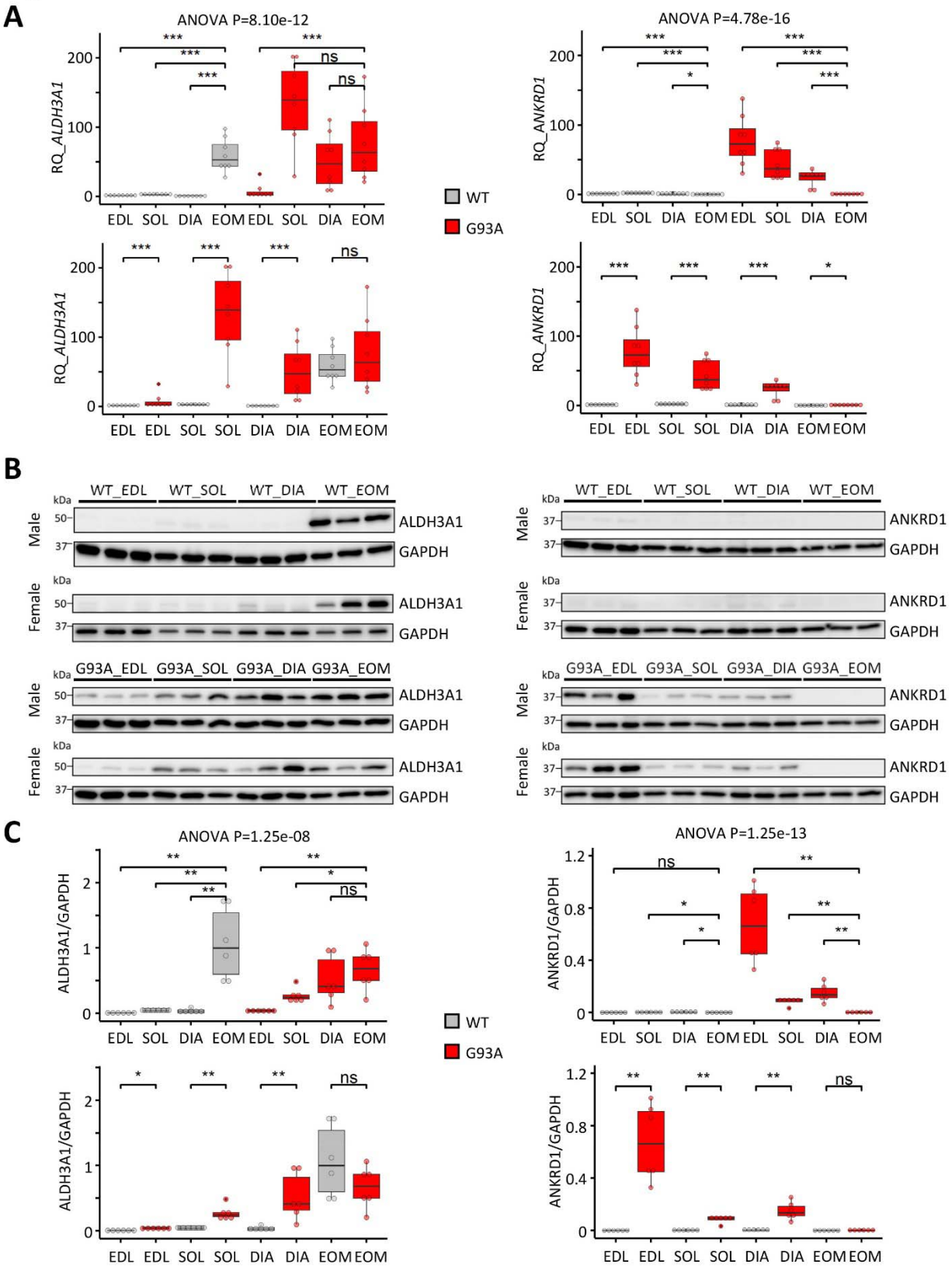

Figure 1. Differential expression of *ALDH3A1* and *ANKRD1* in different muscles from end-stage G93A mice and WT littermates. (**A**) Comparing RNA levels of *ALDH3A1* and *ANKRD1* in Extensor Digitorum Longus (EDL), soleus (SOL), diaphragm (DIA) to those in extraocular muscles (EOMs) by qRT-PCR. N = 8 (4 pairs of male and 4 pairs of female). RQ, relative quantification. *** P < 0.001; * P < 0.05; ns, not significant (Wilcoxon rank-sum test). ANOVA P values are also shown. Please also see **Figure 1-figure supplement 1** and **Figure 1-Source Data 1**. (**B**) Exemplary Western blots of ALDH3A1, ANKRD1 and housekeeping protein GAPDH in different muscles from end-stage G93A mice and WT littermates. N = 6 (3 pairs of male and 3 pairs of female). (**C**) Quantification results of Western blots. * P < 0.05; ** P < 0.01; ns, not significant (Wilcoxon rank-sum test). ANOVA P values are also provided. Please also see **Figure 1-figure supplement 2** and **Figure 1-Source Data 2**.

Figure 2

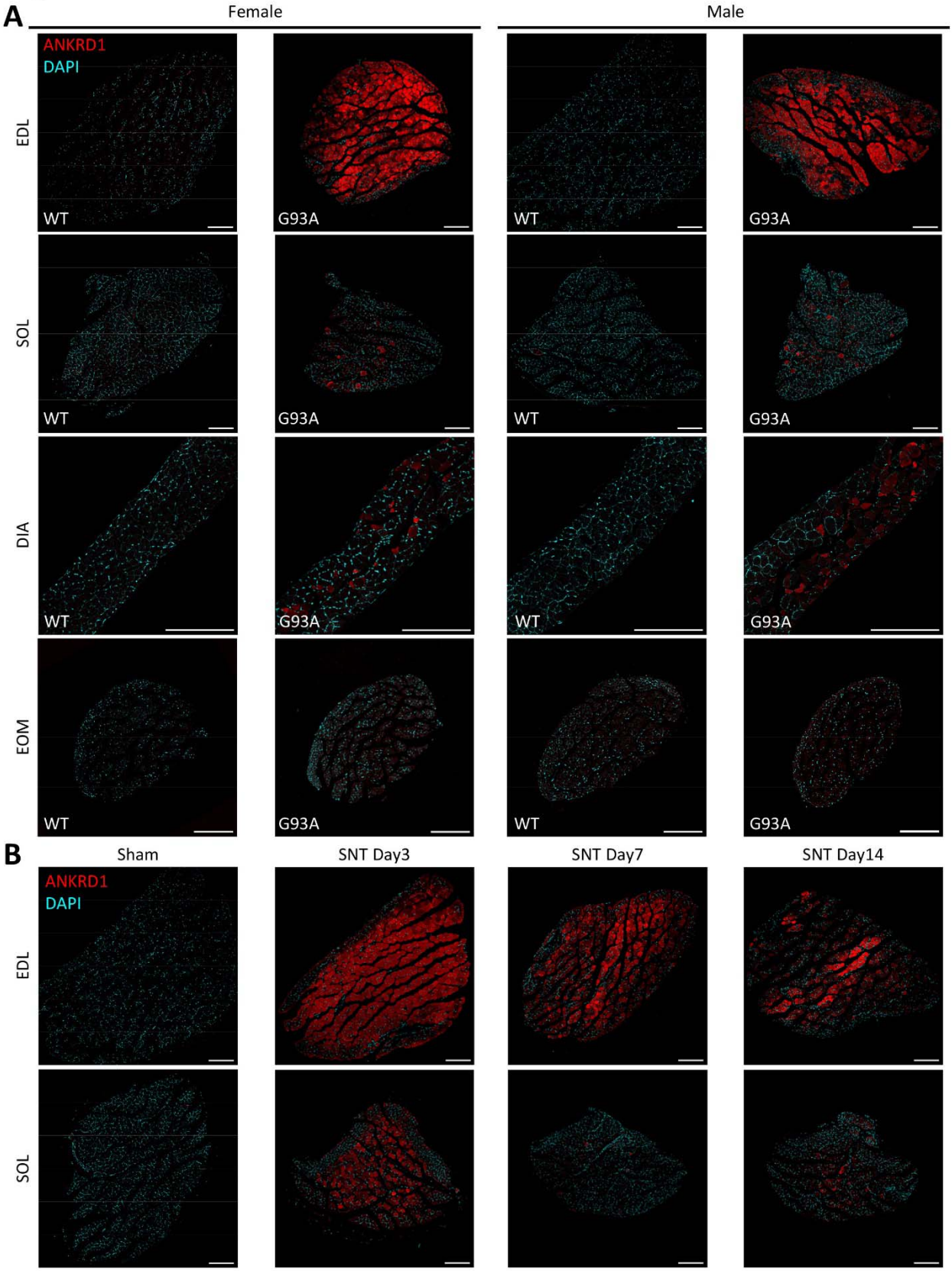

Figure 2. Global view of ANKRD1 immunostaining patterns in transverse sections of different muscles. (**A**) Transverse sections of glyoxal fixed muscles from end-stage G93A mice and WT controls stained with anti-ANKRD1 antibodies and counterstained with DAPI. N = 6 (3 pairs of male and 3 pairs of female). Scale bars, 200 µm. (**B**) Transverse sections of glyoxal fixed EDL and soleus muscles dissected from WT mice (4-5 months of age) at Day 3, Day 7 and Day 14 post sciatic nerve transection and sham operated controls stained with ANKRD1 antibodies and counterstained with DAPI. N = 6 (3 male and 3 female). Scale bars, 200 µm.

Figure 3

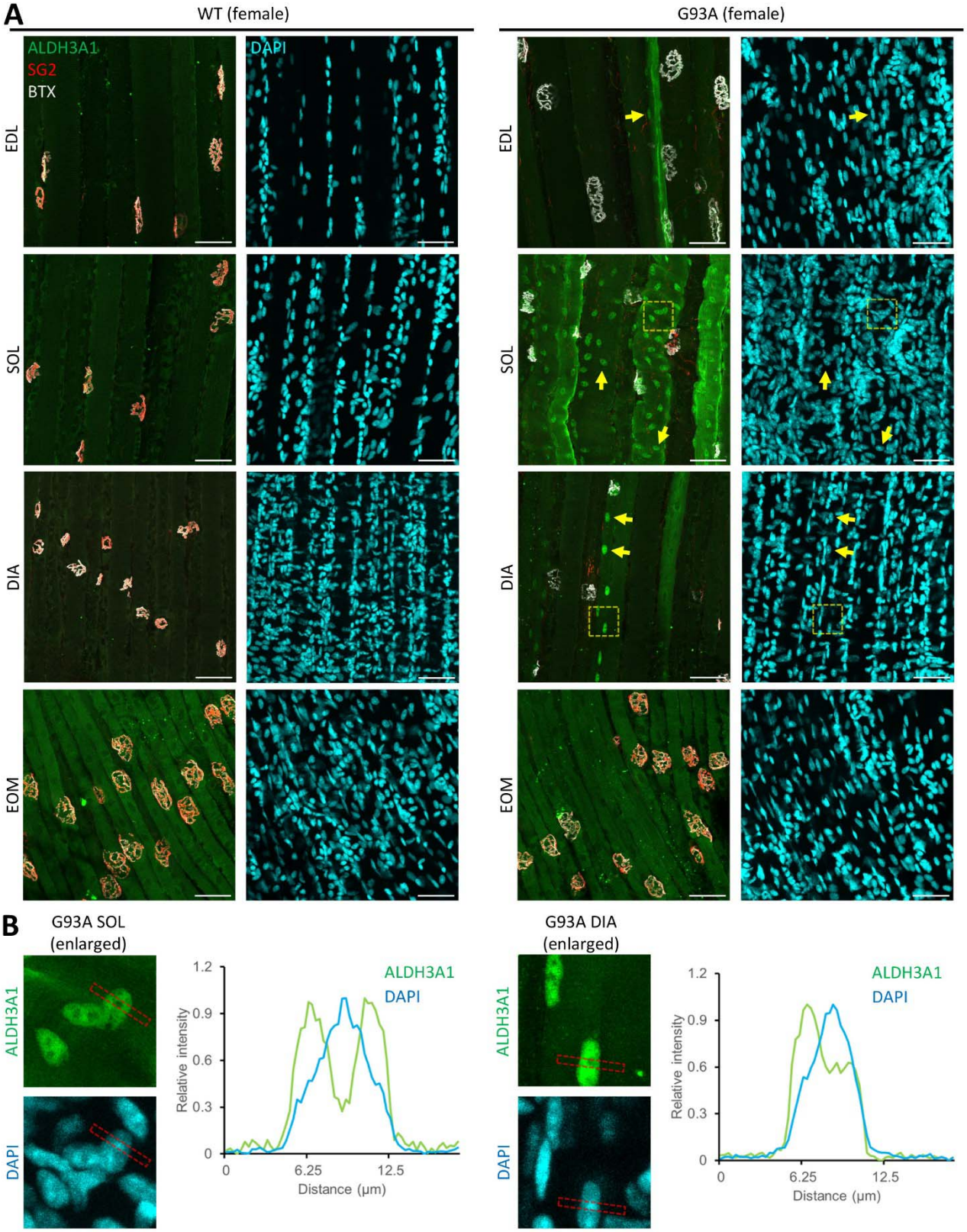

Figure 3. Whole-mount immunostaining of ALDH3A1 in different muscles from end-stage G93A mice and WT littermates. (**A**) Representative compacted z-stack scan images of whole-mount EDL, soleus diaphragm extraocular muscles stained with antibodies against ALDH3A1, SG2 (labeling axon terminals), Alexa Fluor conjugated α-Bungarotoxin (BTX, labeling AChRs on muscle membrane) and DAPI (labeling nuclei). Yellow arrows highlight nuclei with ALDH3A1 enrichment. Dashed yellow boxes denote regions enlarged in Panel B for kymographic measurement. N = 6 (3 pairs of male and 3 pairs of female). Scale bars, 50 μm. Please also see **Figure 3-figure supplement 1A**. (**B**) Profiling the relative intensity of ALDH3A1 and DAPI fluorescent signals along the strips denoted by dashed red boxes. Relative intensities are calculated as $(F - F_{min})/(F_{max} - F_{min})$. Also see **Figure 3-figure supplement 1B**.

Figure 4

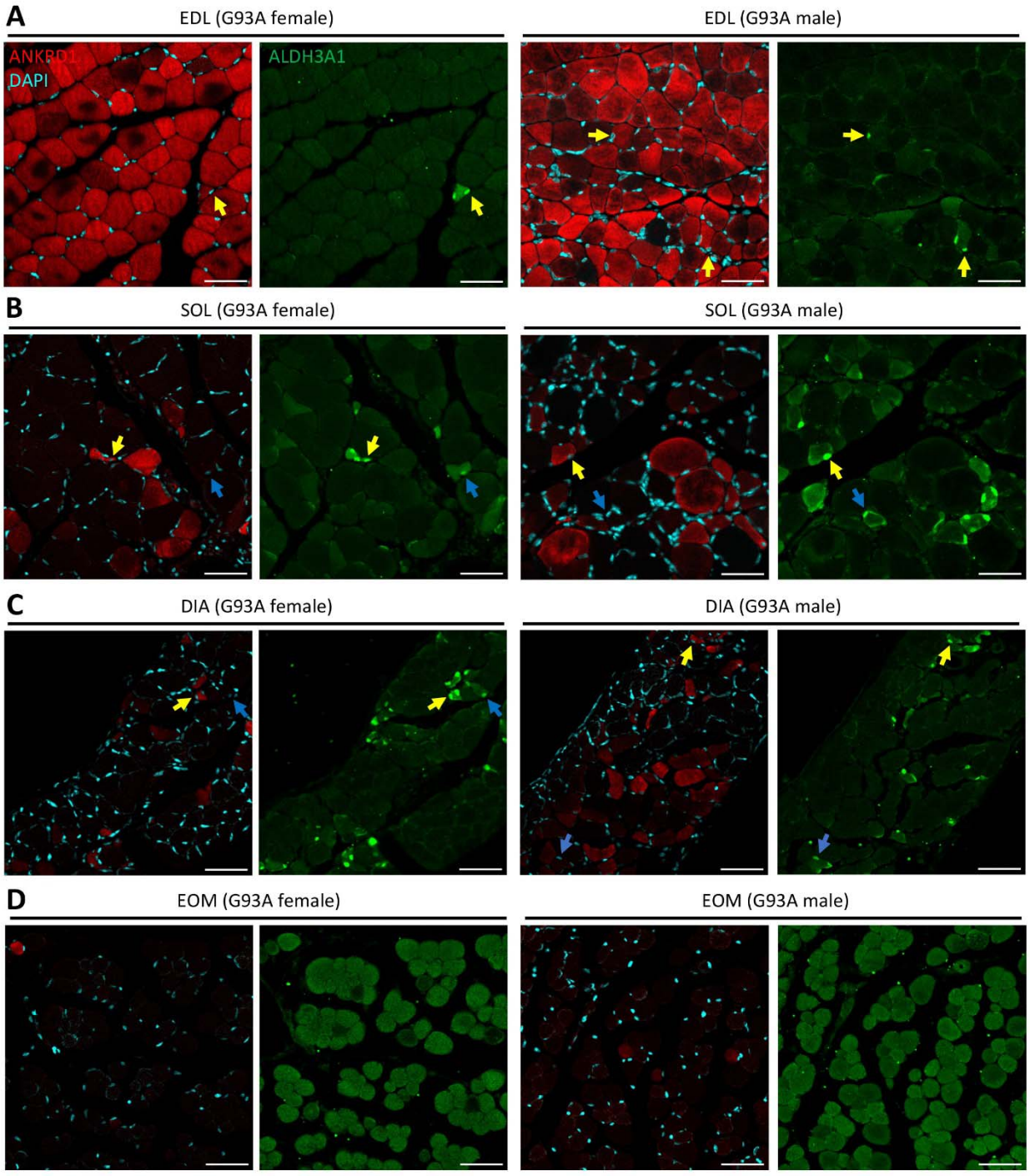

Figure 4. Section immunostaining results of ALDH3A1 and ANKRD1 in different muscles from end-stage G93A mice. (**A-D**) Transverse sections of glyoxal fixed EDL, soleus, diaphragm and EOMs from end-stage G93A mice stained with antibodies recognizing ALDH3A1 and ANKRD1. Yellow arrows denote ALDH3A1 positive myofibers also positive for ANKRD1. Blue arrows denote ALDH3A1 positive myofibers negative for ANKRD1. N = 6 (3 male and 3 female). Scale bars: 50 μm. Please also see **Figure 4-figure supplement 1** for section immunostaining results of ALDH3A1 in WT muscles.

Figure 5

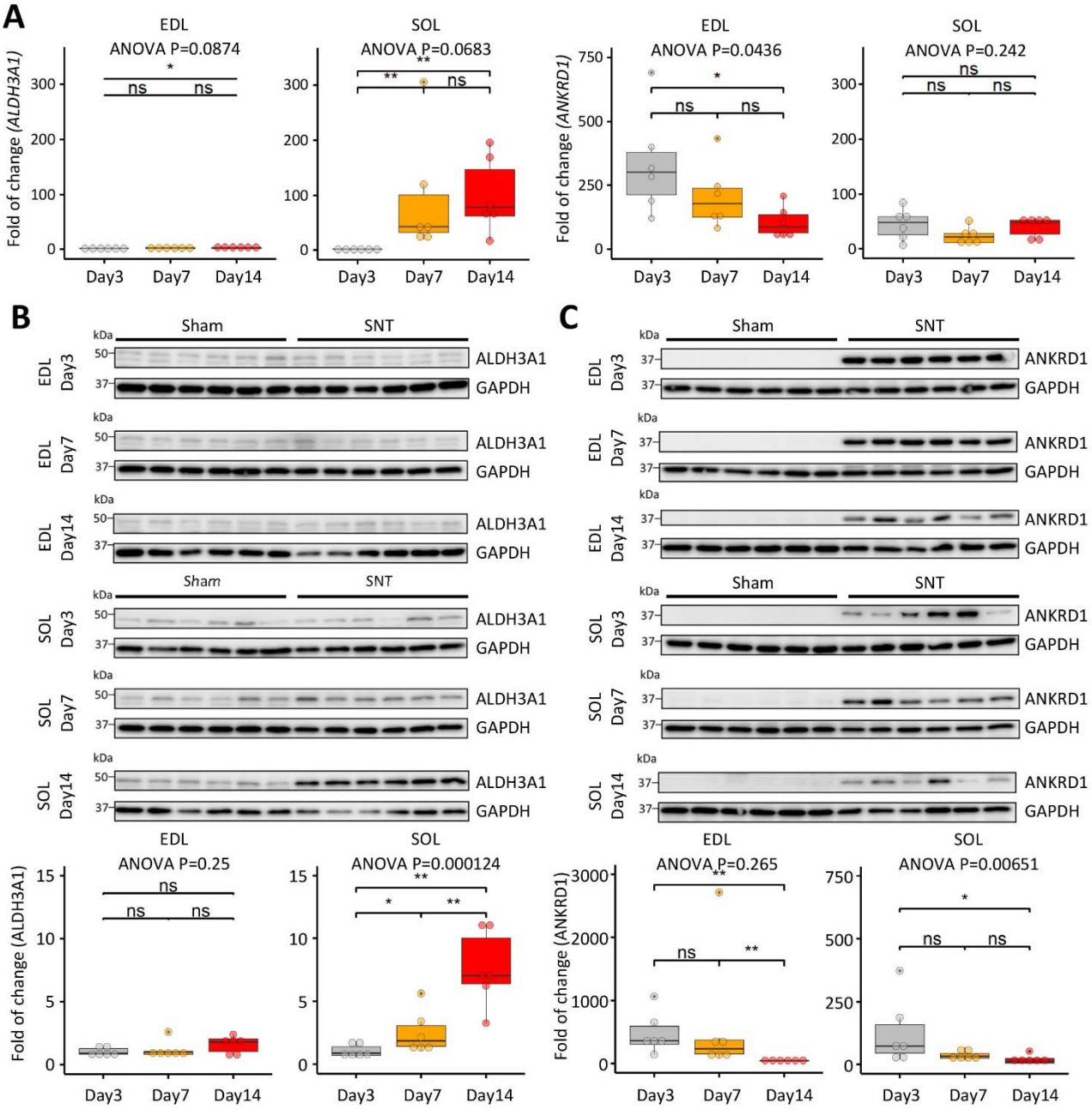

744 **Figure 5. Time and muscle-dependent change of ALDH3A1 abundance after sciatic nerve**
745 **transection.** (**A**) Comparing the changes of *ALDH3A1* and *ANKRD1* expression levels in EDL and
746 SOL from WT mice (4-5 months of age) collected 3 days, 7 days and 14 days after sciatic nerve
747 transection (SNT). Fold of change refers to expression level differences between muscles with SNT
748 and their sham-operated controls examined by qRT-PCR. N = 6 (3 male and 3 female). * $P < 0.05$; **
749 $P < 0.01$; ns, not significant (Wilcoxon rank-sum test). ANOVA P values are also shown. Please also
750 see **Figure 5-Source Data 1**. (**B, C**) Comparing relative changes of ALDH3A1 and ANKRD1 protein
751 (normalized by housekeeping protein GAPDH) in EDL and soleus (SOL) at 3 days, 7 days and 14
752 days after SNT to corresponding sham-operated controls by Western blot. N = 6 (3 male and 3
753 female). * $P < 0.05$; ** $P < 0.01$; ns, not significant (Wilcoxon rank-sum test). ANOVA P values are
754 also shown. Please also see **Figure 5-figure supplement 1** and **Figure 5-Source Data 2, 3**.

Figure 6

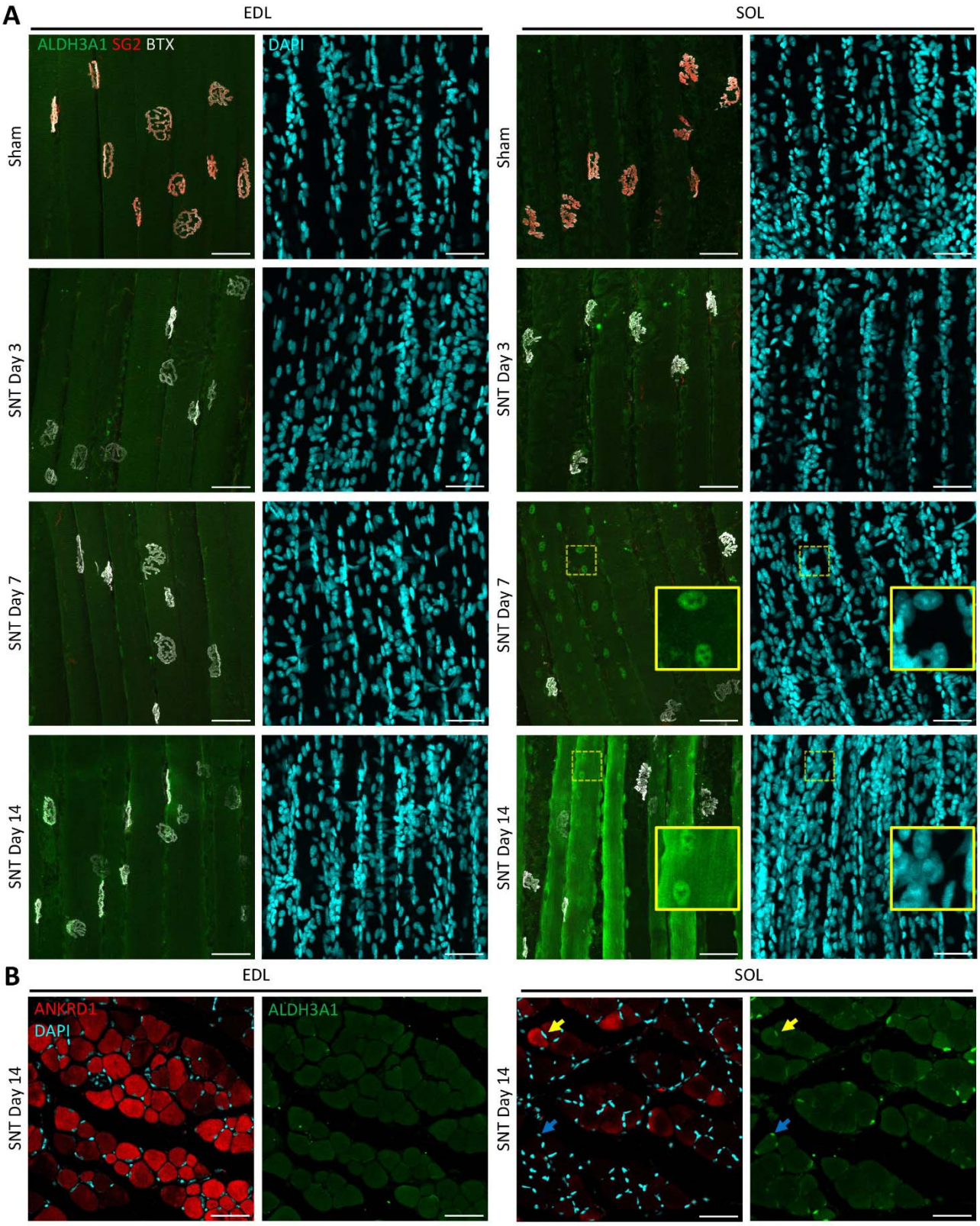

Figure 6. Examining subcellular distribution of ALDH3A1 protein in EDL and soleus muscles from WT mice with sciatic nerve transection. (**A**) Examining subcellular distribution of ALDH3A1 in EDL and soleus (SOL) muscles collected 3 days, 7 days and 14 days after SNT and sham-operated controls by whole-mount immunostaining. Antibodies against SG2 labels axon terminals at NMJ and Alexa Fluor tagged BTX labels AChRs on the sarcolemma at NMJ. Regions denoted by dashed yellow boxes are enlarged in insets. N = 6 (3 male and 3 female). Scale bars: 50 μm. (**B**) Transverse sections of glyoxal fixed EDL and soleus muscles collected 14 days after SNT stained with ANKRD1, ALDH3A1 antibodies and DAPI. Yellow arrows denote ALDH3A1 positive myofibers also positive for ANKRD1. Blue arrows denote ALDH3A1 positive myofibers negative for ANKRD1. Scale bars: 50 μm.

Figure 7

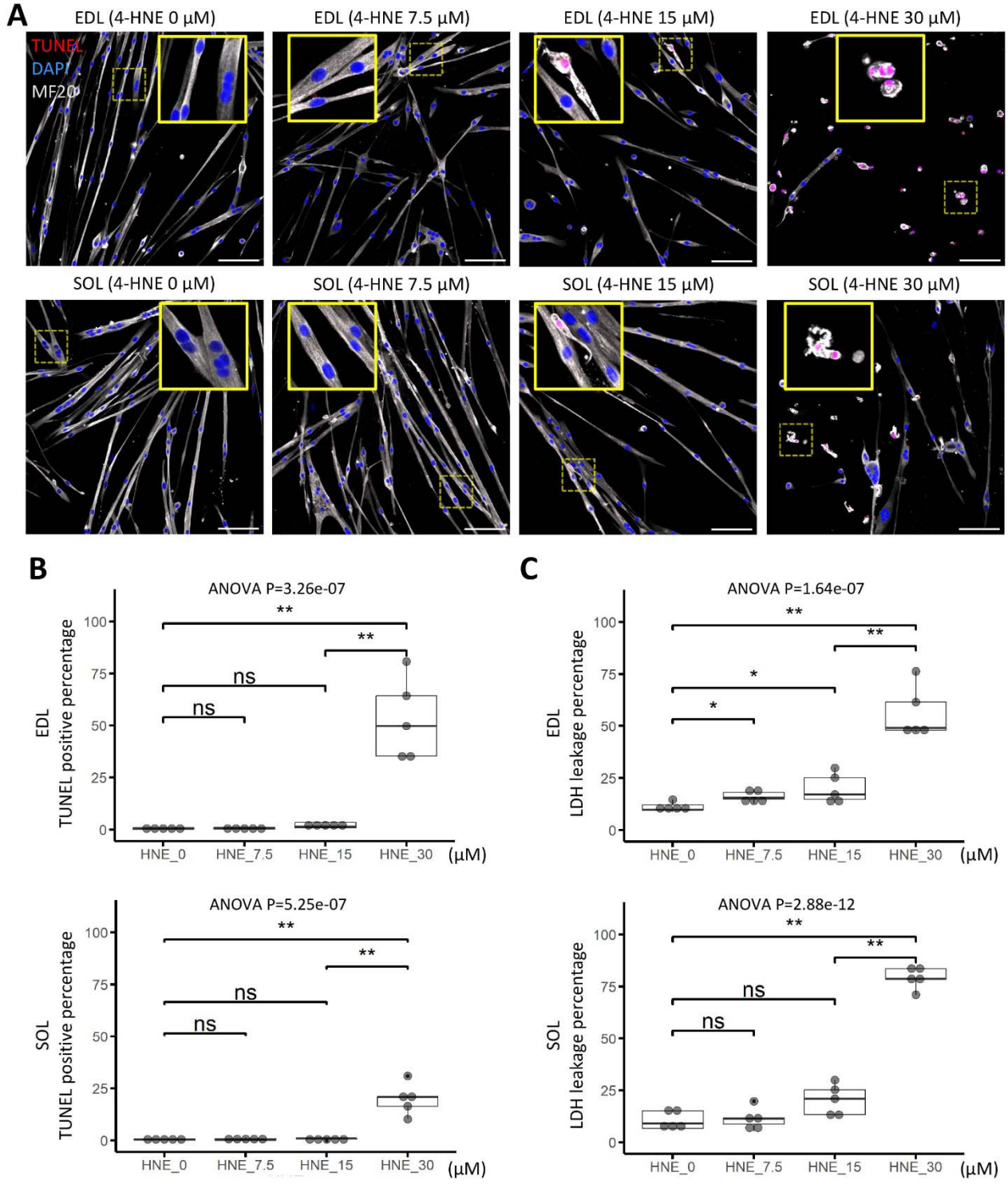

Figure 7. Characterizing 4-HNE cytotoxicity to myotubes derived from EDL and soleus satellite cells. (**A**) Myotubes differentiated from EDL or soleus satellite cells isolated from 4-month-old WT female mice for 5 days were treated with 0, 7.5, 15 or 30 μM 4-HNE for 2 hrs, respectively. Afterwards the myotubes were cultured for another 16 hrs in regular differentiation medium (as apoptosis takes time to occur) before fixation, TUNEL staining and immunostaining against MF-20 (labeling the cytosolic part of myotubes). DAPI counterstaining labelled the nuclei. N = 3 culture replicates. Regions denoted by dashed yellow boxes are enlarged in insets. Scale bars: 100 μm. (**B**) Averaged TUNEL positive percentage of nuclei in myotubes treated with different concentrations of 4-HNE (N = 5 culture replicates, 4 images analyzed and averaged for each culture replicate). ** P < 0.01; ns, not significant (t.test). ANOVA P values are also shown. Please also see **Figure 7-Source Data 1**. (**C**) Measuring 4-HNE cytotoxicity to myotubes using LDH leakage-based assay (N = 5 culture replicates). ** P < 0.01; * P < 0.05; ns, not significant (Wilcoxon rank-sum test). ANOVA P values are also shown. Please also see **Figure 7-Source Data 2**.

Figure 8

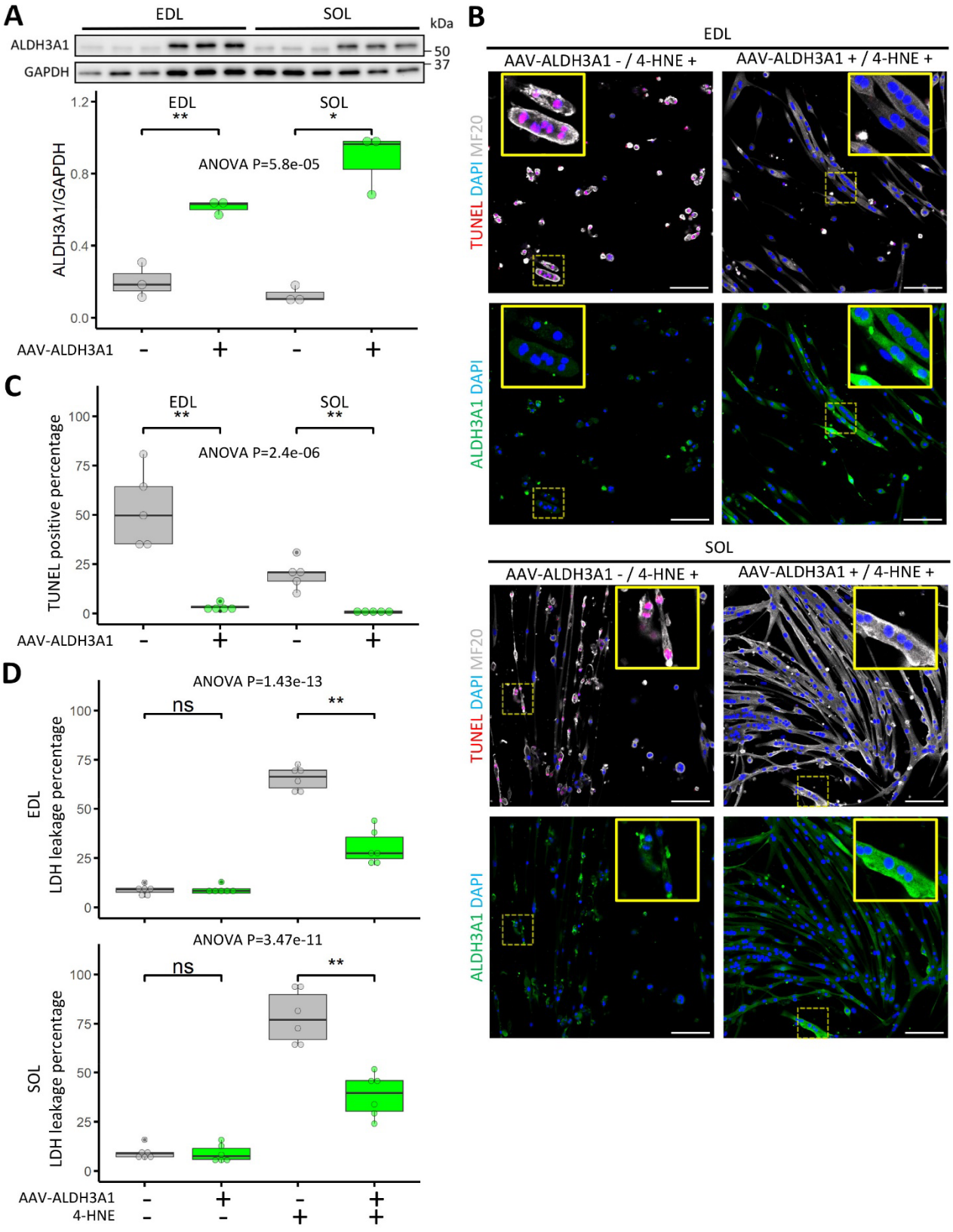

Figure 8. Transducing myotubes with AAV-ALDH3A1 protects against 4-HNE cytotoxicity. (**A**) Myotubes differentiated from EDL or soleus satellite cells for 1 day (isolated from 4-month-old WT female mice) were incubated with or without AAV-ALDH3A1 for 2 days, followed by another 2-day culture in regular differentiation medium before protein extraction and Western blot. N = 3 culture replicates. ** P < 0.01; * P < 0.05 (t-test). Please also see **Figure 8-Source Data 1**. (**B**) Myotubes differentiated from EDL or soleus satellite cells isolated from 4-month-old female WT mice with or without AAV-ALDH3A1 transduction were treated with 30 μM 4-HNE for 2 hrs. Afterwards the myotubes were cultured for another 16 hrs in regular differentiation medium before fixation, TUNEL staining, immunostaining against MF-20 (labeling the cytosolic part of myotubes) and ALDH3A1. DAPI counterstaining labelled the nuclei. N = 3 culture replicates. Regions denoted by dashed yellow boxes are enlarged in insets. Scale bars: 100 μm. (**C**) Quantification results of averaged TUNEL positive percentage of nuclei in myotubes (N = 3 culture replicates, 4 images analyzed and averaged for each culture replicate). ANOVA P values are also shown. * P < 0.05 (t-test). Please also see **Figure 8-Source Data 2**. (**D**) Measuring the protective effect of AAV-ALDH3A1 against 4-HNE cytotoxicity to myotubes using LDH leakage-based assay (N = 6 culture replicates). ** P < 0.01; ns, not significant (Wilcoxon rank-sum test). ANOVA P values are also shown. Please also see **Figure 8-Source Data 3**.

Figure 9

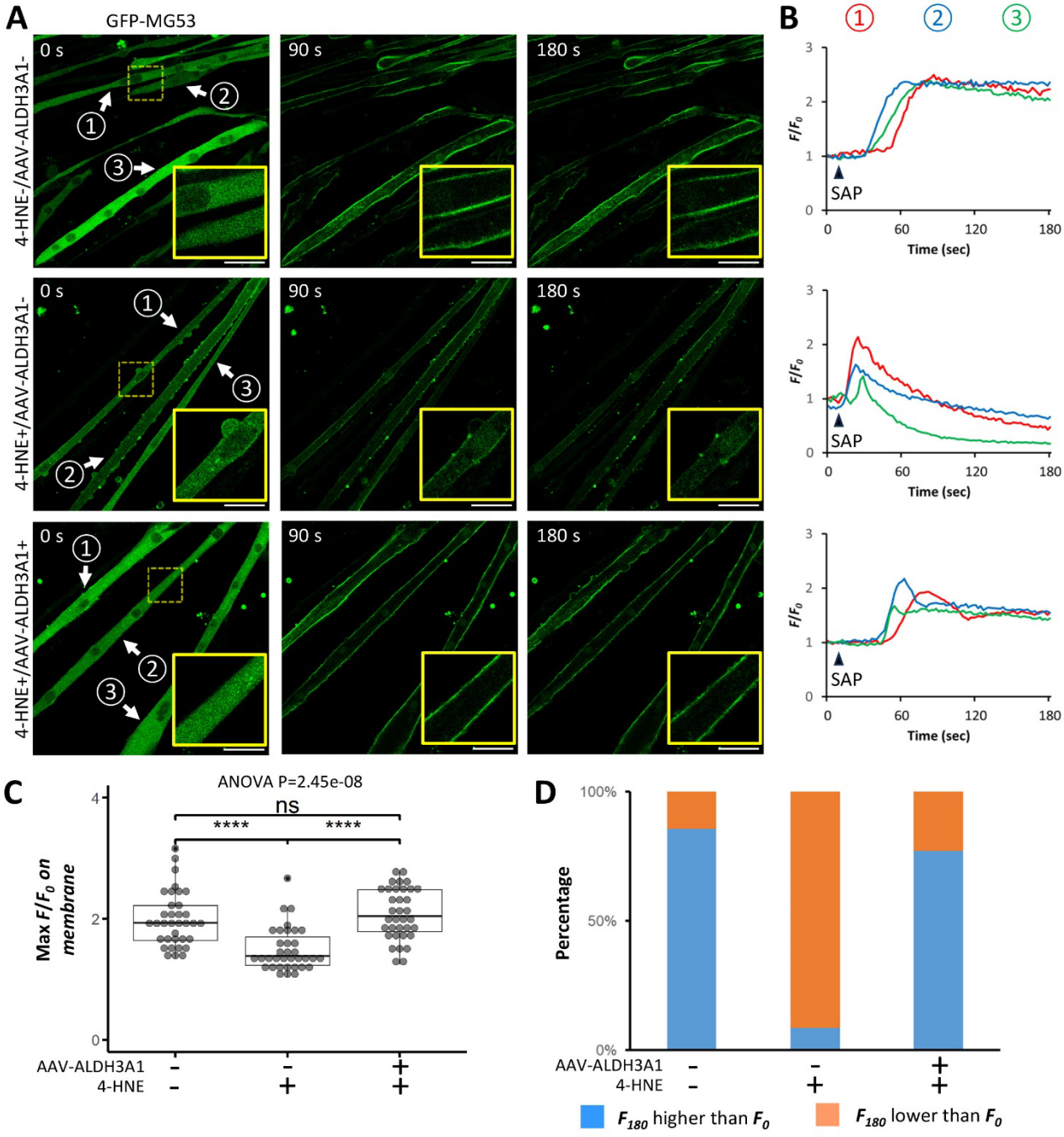

Figure 9. AAV-ALDH3A1 protects against 4-HNE compromised stabilization of MG53 repair patches in partially permeabilized myotubes. (**A**) Time lapse imaging of saponin-induced formation of GFP-MG53 repair patches on the plasma membrane in soleus satellite cell derived myotubes with or without AAV-ALDH3A1 transduction and/or 4-HNE treatment (30 μM for 2 hrs). Regions denoted by dashed yellow boxes are enlarged in insets. Arrows highlight myotubes whose GFP-MG53 intensity on the plasma membrane were profiled in panel B. Scale bars: 50 μm. Please also see Videos 1-3. (**B**) Plotting background-corrected, initial timepoint intensity normalized signal of GFP-MG53 on plasma membrane (F/F_0) over time for the three myotubes indicated in Panel A. Arrowheads denote the time point when saponin was applied. (**C**) Maximum F/F_0 of recorded myotubes under different treatment conditions (N = 35 for each group). **** P < 0.0001; ns, not significant (Wilcoxon rank-sum test). ANOVA P values are also shown. Please also see **Figure 9-Source Data 1**. (**D**) Percentage stacked column chart highlights the proportion of recorded myotubes with F_{180} (end of recording) higher than F_0 (blue) and the proportion of those with F_{180} lower than F_0 (orange) in different treatment groups. Please also see **Figure 9-source data 1**.

Video 1. Time lapse imaging of GFP-MG53 transfected myotubes without 4-HNE or AAV-ALDH3A1 treatment.

Video 2. Time lapse imaging of GFP-MG53 transfected myotubes treated with 30 μM 4-HNE for 2 hours before recording.

Video 3. Time lapse imaging of GFP-MG53 transfected, AAV-ALDH3A1 transduced myotubes treated with 30 μM 4-HNE for 2 hours before recording.

Figure 1-figure supplement 1

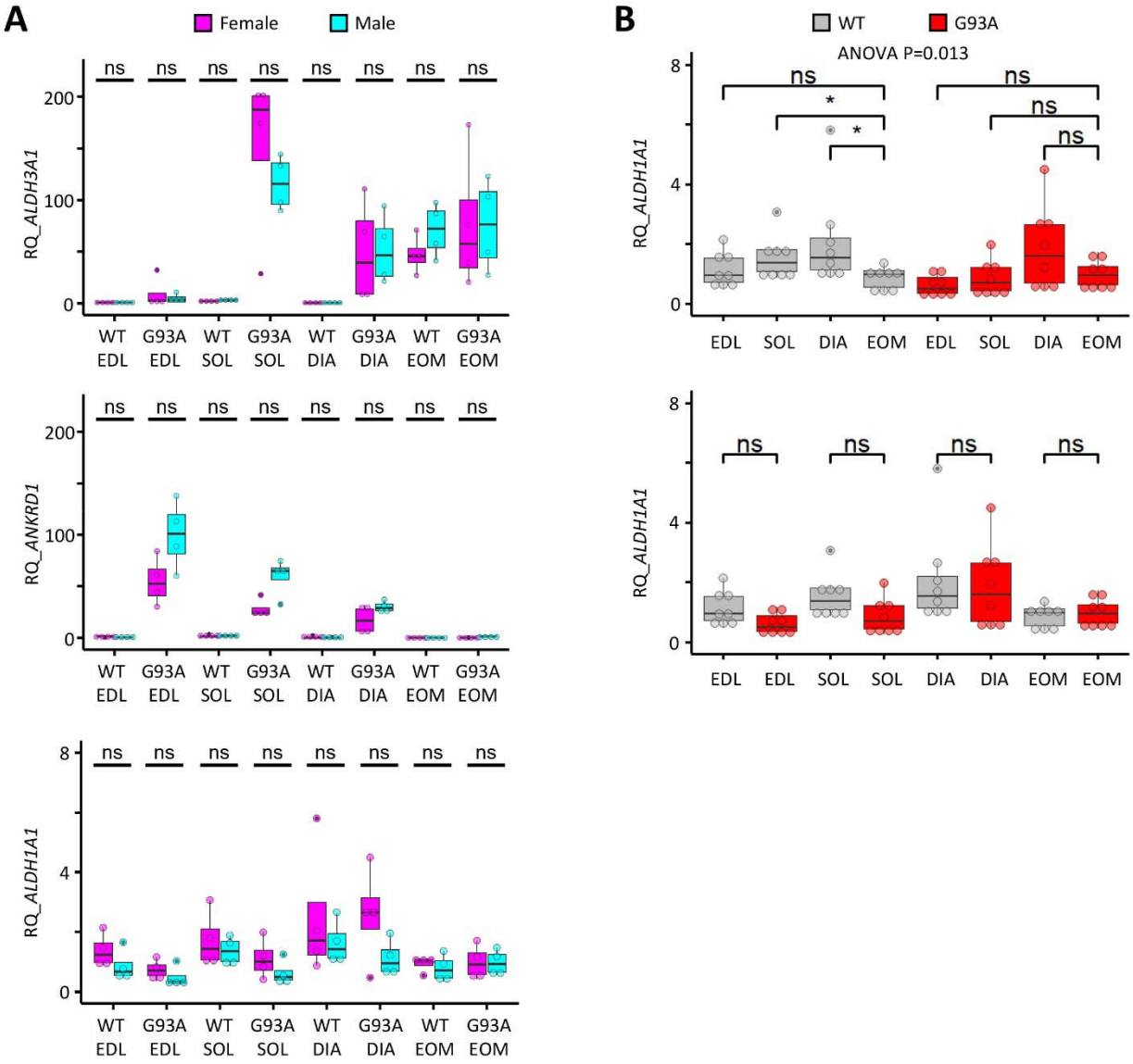

Figure 1-figure supplement 1. Additional qRT-PCR results for *ALDH1A1*, *ALDH3A1* and *ANKRD1* expression in different muscles from end-stage G93A mice and WT littermates. (**A**) qRT-PCR results for *ALDH3A1*, *ANKRD1* and *ALDH1A1* separated by gender (magenta: female; cyan: male) and compared through Wilcoxon rank-sum tests (ns, not significant). N = 8 (4 pairs of male and 4 pairs of female). RQ, relative quantification. Please also see Figure 1-Source Data 1. (**B**) Comparing RNA levels of *ALDH1A1* in Extensor Digitorum Longus (EDL), soleus (SOL), diaphragm (DIA) to those in extraocular muscles (EOMs) by qRT-PCR. * $P < 0.05$; ns, not significant (Wilcoxon rank-sum test). ANOVA P values are also shown.

Figure 1-figure supplement 2

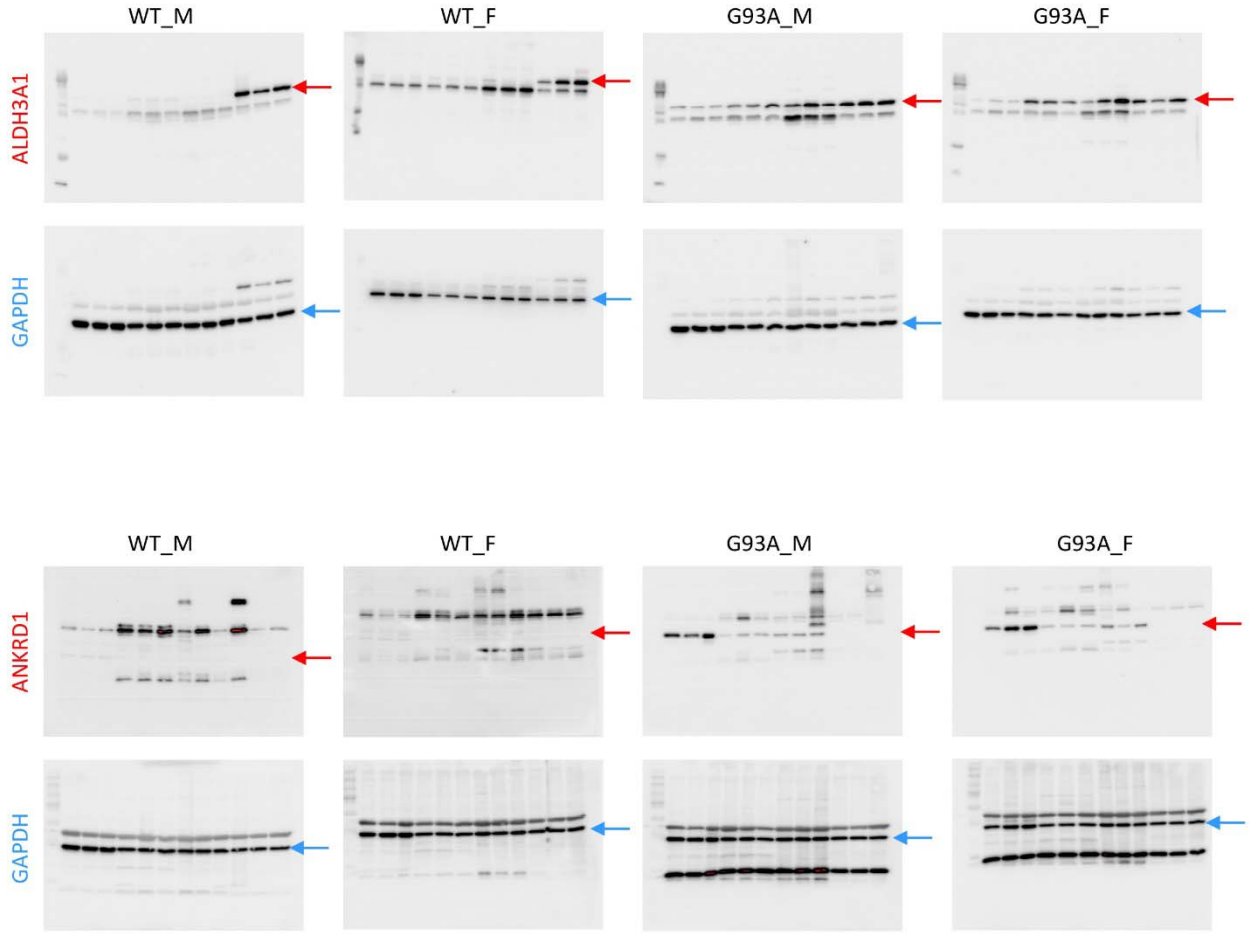

Figure 1-figure supplement 2. Original images for Western blots in Figure 1. Red arrows indicate ALDH3A1 (51 kDa) or ANKRD1 (36 kDa) bands. Blue arrows indicate GAPDH (36 kDa) bands.

Figure 3-figure supplement 1

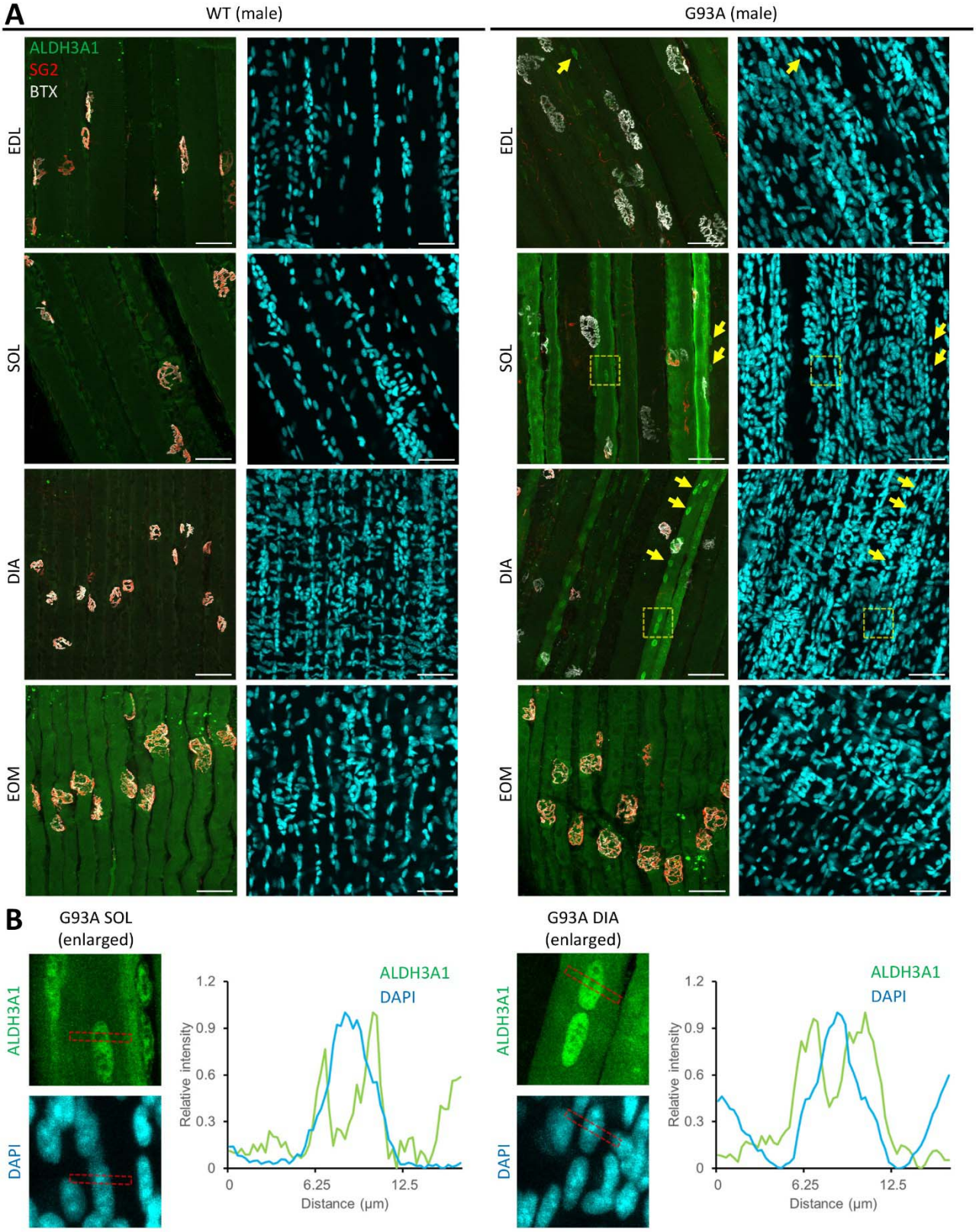

Figure 3-figure supplement 1. Additional images of ALDH3A1 whole-mount immunostaining in different muscles from end-stage G93A mice and WT littermates. (**A**) Representative compacted z-stack scan images of whole-mount EDL, soleus diaphragm extraocular muscles stained with antibodies against ALDH3A1, SG2 (labeling axon terminals), Alexa Fluor conjugated α-Bungarotoxin (BTX, labeling AChRs on muscle membrane) and DAPI (labeling nuclei). N = 6 (3 pairs of male and 3 pairs of female). Scale bars, 50 μm. Yellow arrows highlight nuclei with ALDH3A1 enrichment. Dashed yellow boxes denote regions enlarged in Panel B for kymographic measurement. (**B**) Profiling the relative intensity of ALDH3A1 and DAPI fluorescent signals along the strips denoted by the red boxes. Relative intensities are calculated as $(F - F_{min})/(F_{max} - F_{min})$.

Figure 4-figure supplement 1

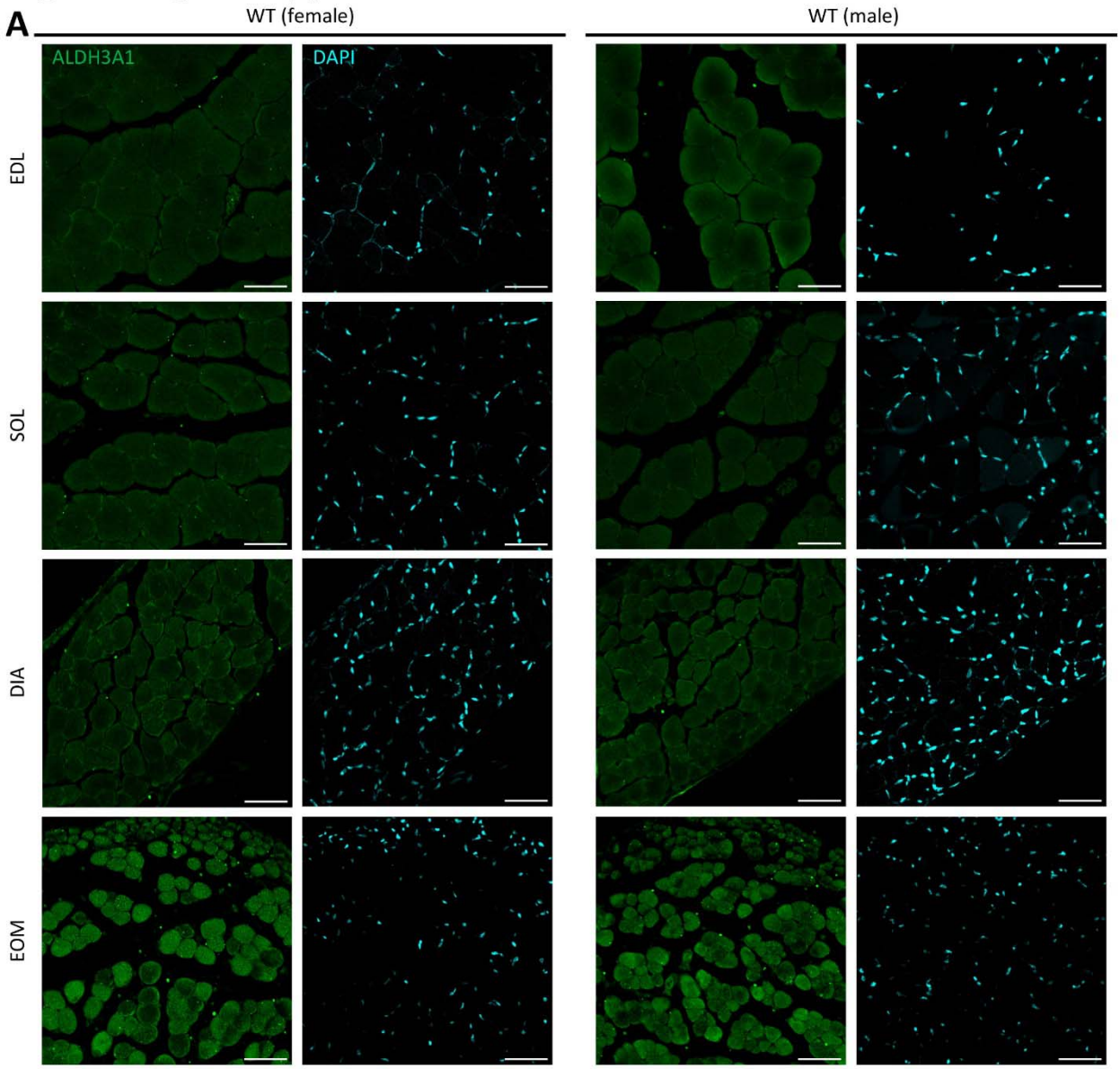

Figure 4-figure supplement 1. Section immunostaining results of ALDH3A1 in different muscles from WT mice 4-5 months of age. (**A**) Transverse sections of glyoxal fixed EDL, soleus, diaphragm and EOMs from WT mice stained with antibodies recognizing ALDH3A1. N = 6 (3 male and 3 female). Scale bars: 50 μm.

Figure 6-figure supplement 1

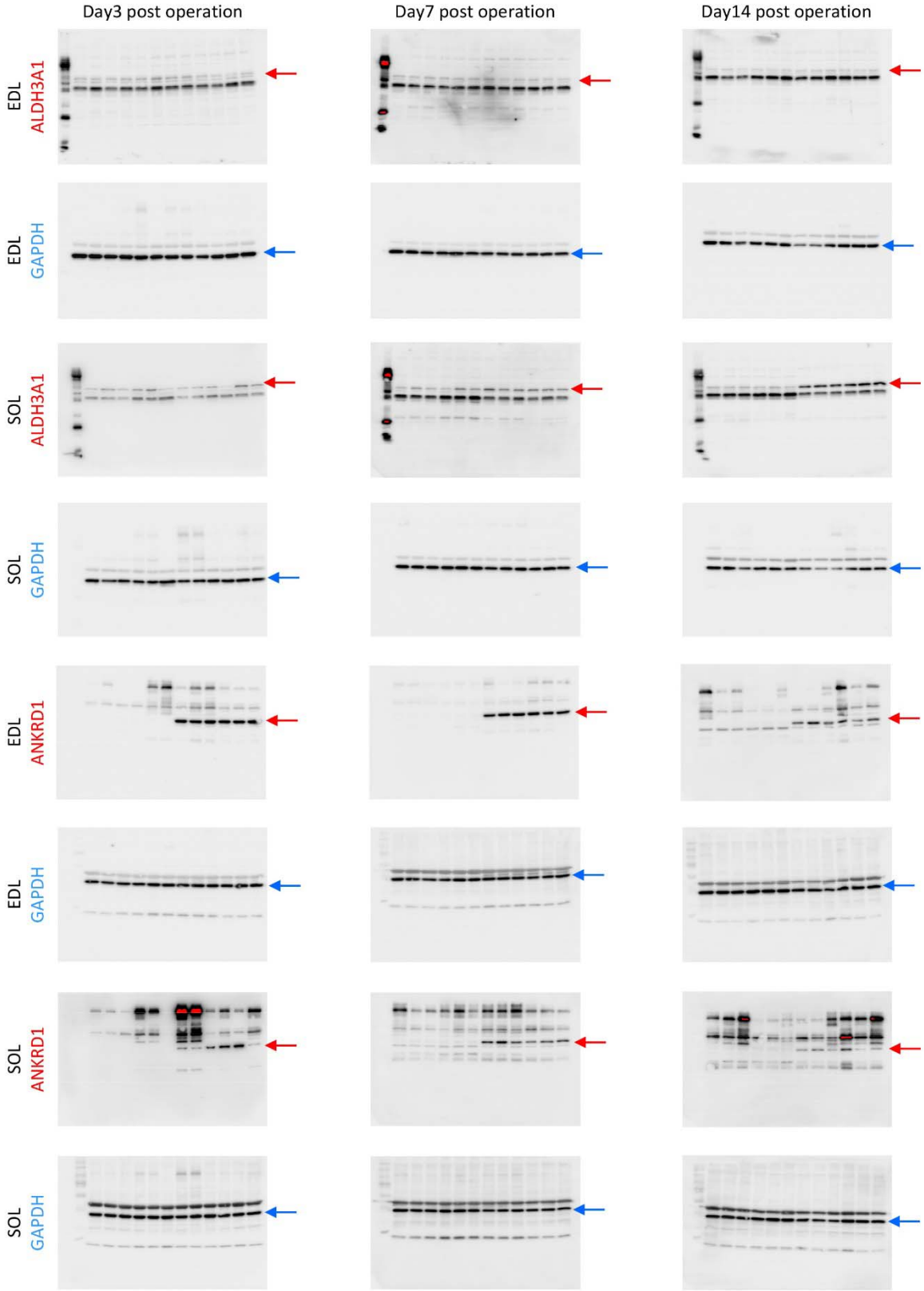

Figure 6-figure supplement 1. Original images of Western blots in Figure 6. Red arrows indicate ALDH3A1 (51 KDa) or ANKRD1 (36 kDa) bands. Blue arrows indicate GAPDH (36 kDa) bands.

Figure 1-Source Data 1. qRT-PCR results for *ALDH1A1*, *ALDH3A1* and *ANKRD1* relative expression levels in whole muscles of different origins.

Figure 1-Source Data 2. Western blot quantification results for ALDH3A1 and ANKRD1 protein levels in whole muscles of different origins.

Figure 5-Source Data 1. qRT-PCR results of the fold of change of *ALDH3A1* and *ANKRD1* expression levels in whole muscles with SNT compared to the sham operated controls.

Figure 5-Source Data 2. Western blot quantification results of the fold of change of ALDH3A1 protein levels in whole muscles with SNT compared to the sham operated controls.

Figure 5-Source Data 3. Western blot quantification results of the fold of change of ANKRD1 protein levels in whole muscles with SNT compared to the sham operated controls.

Figure 7-Source Data 1. Quantification results of the percentages of TUNEL positive nuclei in myotubes treated with different concentrations of 4-HNE.

Figure 7-Source Data 2. Quantification results of LDH leakage percentages of myotubes treated with different concentrations of 4-HNE.

Figure 8-Source Data 1. Western blot quantification results for ALDH3A1 protein levels in myotubes with or without transduction of AAV-ALDH3A1.

Figure 8-Source Data 2. Quantification results of the percentages of TUNEL positive nuclei in myotubes with or without transduction of AAV-ALDH3A1 before 4-HNE treatment.

Figure 8-Source Data 3. Quantification results of LDH leakage percentages of myotubes with or without transduction of AAV-ALDH3A1 before 4-HNE treatment.

Figure 9-Source Data 1. Ratios between maximum *F* and F_0 in each recorded myotubes transfected with GFP-MG53 and whether the F_{180} is higher or lower than F_0.